# A Spatiotemporal Constrained Machine Learning Method for OCO-2 Solar-Induced Chlorophyll Fluorescence (SIF) Reconstruction

Huanfeng Shen, *Senior Member, IEEE*, Yuchen Wang, Xiaobin Guan, Wenli Huang, *Member, IEEE*,
Jiajia Chen, Dekun Lin, and Wenxia Gan, *Member, IEEE*

***Abstract*— Solar-induced chlorophyll fluorescence (SIF) is an intuitive and accurate way to measure vegetation photosynthesis. Orbiting Carbon Observatory-2 (OCO-2)-retrieved SIF has shown great potential in estimating terrestrial gross primary production (GPP), but the discontinuous spatial coverage limits its application. Although some researchers have reconstructed OCO-2 SIF data, few have considered the uneven spatial and temporal distribution of the swath-distributed data, which can induce large uncertainties. In this article, we propose a spatiotemporal constrained light gradient boosting machine model (ST-LGBM) to reconstruct a contiguous OCO-2 SIF product (eight days, 0.05°), considering the data distribution characteristics. Two spatial and temporal constraining factors are introduced to utilize the relationships between the swath-distributed OCO-2 samples, combining the geographical regularity and vegetation phenological characteristics. The results indicate that the ST-LGBM method can improve the reconstruction accuracy in the missing data areas ($R^2 = 0.79$), with an increment of 0.05 in $R^2$. The declined accuracy of the traditional light gradient boosting machine (LightGBM) method in the missing data areas is well alleviated in our results. The real-data comparison with TROPOspheric Monitoring Instrument (TROPOMI) SIF observations also shows that the results of the ST-LGBM method can achieve a much better consistency, in both spatial distribution and temporal variation. The sensitivity analysis also shows that the ST-LGBM can support stable results when using various input combinations or different machine learning models. This approach represents an innovative way to reconstruct a more accurate globally continuous OCO-2 SIF product and also provides references to reconstruct other data with a similar distribution.**

Manuscript received 13 March 2022; revised 31 July 2022; accepted 30 August 2022. Date of publication 8 September 2022; date of current version 23 September 2022. This work was supported in part by the National Key Research and Development Program of China under Grant 2019YFB2102903, in part by the National Natural Science Foundation of China under Grant 42001371, and in part by the Fundamental Research Funds for Central Universities under Grant 2042022kf1070. *(Corresponding author: Xiaobin Guan.)*

Huanfeng Shen is with the School of Resource and Environmental Sciences and the Collaborative Innovation Center of Geospatial Technology, Wuhan University, Wuhan 430079, China (e-mail: shenhf@whu.edu.cn).

Yuchen Wang, Xiaobin Guan, Wenli Huang, Jiajia Chen, and Dekun Lin are with the School of Resource and Environmental Science, Wuhan University, Wuhan 430079, China (e-mail: wangyuchencyhl@whu.edu.cn; guanxb@whu.edu.cn; wenli.huang@whu.edu.cn; evechen@whu.edu.cn; lindekun@whu.edu.cn).

Wenxia Gan is with the School of Civil Engineering and Architecture, Wuhan Institute of Technology, Wuhan 430205, China (e-mail: charlottegan@whu.edu.cn).

This article has supplementary downloadable material available at https://doi.org/10.1109/TGRS.2022.3204885, provided by the authors.

Digital Object Identifier 10.1109/TGRS.2022.3204885

***Index Terms*— Machine learning, Orbiting Carbon Observatory-2 (OCO-2), solar-induced chlorophyll fluorescence (SIF), spatiotemporal constraint.**

## I. INTRODUCTION

PHOTOSYNTHESIS, which is the fundamental and intricate physiological process of vegetation, is one of the key factors of the global carbon cycle [1]. Gross primary productivity (GPP), which is the amount of organic carbon fixed by plants per unit of time, represents the photosynthetic carbon uptake of the terrestrial ecosystem [2]. Previous studies have made considerable efforts to quantify terrestrial GPP, and a large number of models have been developed, including data-driven models [3], process-based models [4], and light-use efficiency models [5]. Although these models can acquire multiscale GPP simulations with varied accuracy when combined with remote sensing technology, they are usually impacted by model complexity, parameter uncertainty, and assumption differences [6]. Solar-induced chlorophyll fluorescence (SIF), which is the phenomenon of energy released in a long-wave manner during photosynthesis [7], is a new way to study terrestrial plants. Several studies over the last decade have reported a strong relationship between GPP and SIF, showing the great potential of SIF to estimate GPP with a high degree of accuracy [8], [9].

Numerous hyperspectral satellites have been launched into space over the last decades, making large-scale and global SIF inversion possible. Several SIF products have been released with different spatial and temporal resolutions, such as the products produced by the Scanning Imaging Absorption SpectroMeter for Atmospheric ChartogrphY (SCIAMACHY) [10], the Global Ozone Monitoring Experiment-2 (GOME-2) [11], the Greenhouse Gases Observing SATellite (GOSAT) [10], the Orbiting Carbon Observatory-2 (OCO-2) [12], and the TROPOspheric Monitoring Instrument (TROPOMI) [13]. These products have been widely used to monitor vegetation photosynthesis at different scales [14], [15], based on their various application scenarios and requirements. Among the different products, the SCIAMACHY (30 × 240 km), GOME-2 (40 × 80 km), and GOSAT (10 km) products, which are early SIF products, can provide long-term coverage. However, they cannot meet the needs of vegetation research at a regional scale because they are limited by the coarse resolution and huge data uncertainties. The TROPOMI instrument on board the Sentinel-5 Precursor satellite, which was launched in October 2017, is the newest instrument that can acquire finer observations, with a minimum footprint of 5.5 × 3.5 $\mathrm{km}^2$ and a daily revisit cycle. Nevertheless, it cannot support vegetation monitoring over a long time scale [16]. The OCO-2 satellite, which was launched in July 2014, is the first specialized satellite to study atmospheric carbon dioxide from space. Several studies have reported a high correlation between OCO-2 SIF and eddy covariance (EC) GPP [17]. The OCO-2 satellite provides a small spatial footprint that can match the EC flux towers better [18]. Specifically, the spectrometer used for SIF retrieval provides eight independent cross-track spectra, whose spatial resolution (i.e., footprint size) is 1.29 × 2.25 $\mathrm{km}^2$ at nadir and covers an approximately 10-km-wide swath altogether [19]. The data collection characteristics of OCO-2 promise a high data density with a finer resolution [20] and a better signal-to-noise ratio (SNR) [12]. In addition, the Orbiting Carbon Observatory-3 (OCO-3) instrument on board the International Space Station completed its in-orbit checkout in 2019 [21] and continues to provide SIF observations. By using the same core grating spectrometer and applying the same techniques as OCO-2, but with improvements in many areas [21], OCO-3 can be regarded as a supplement and augment to the OCO-2 data record [22]. All of the above indicates the great potential of OCO-2 SIF retrieval in global carbon cycle study [23].

However, limited by the discontinuous and sparse sampling strategy, the OCO-2 SIF product also has a fatal deficiency with regard to its spatiotemporal coverage, which cannot be ignored. Although the footprint of OCO-2 SIF retrieval is less than 2.25-km downtrack, there are massive gaps between adjacent swaths, due to the 16-day revisit cycle and sparse sampling strategy. The huge gaps mean that the results of OCO-2 SIF retrieval are often aggregated to 1° × 1° monthly datasets, losing the high spatial resolution and data density. In order to solve this problem, several reconstruction studies have been completed in recent years to make better use of the OCO-2 SIF product [24], [25], [26], with the aim being to reconstruct the swath-distributed OCO-2 samples into a continuous spatiotemporal distribution. Different continuous products with higher spatiotemporal resolutions have been generated, such as CSIF [25] (0.05°, four days) and GOSIF [26] (0.05°, eight days), which have significantly improved the data availability. These products are usually reconstructed using a data-driven method, combined with remote sensing vegetation indices or reflectance bands and other auxiliary data. Due to the advantages in spatial and temporal continuity and resolution, these reconstructed products have been widely used in vegetation-related studies, including GPP estimation [27], phenology analyses [28], vegetation stress detection [29], and carbon cycle studies [30].

Although these previous OCO-2 reconstruction works have obtained reasonable accuracies, one issue has been ignored, which can induce large uncertainties, that is, none of the previous studies have considered the uneven spatiotemporal distribution of the OCO-2 observations. The sparse sampling strategy of the OCO-2 instrument typically leads to severe gaps in the data, i.e., each swath only contains 2–3 pixels, but the gap between two adjacent swaths covers more than 60 pixels even if aggregated to 0.05°, eight-day gridded data. Hence, there may be no data observed in many regions all year round. In this condition, huge uncertainties exist in these gaps [12], [17], [23] because the relationship trained by the samples from limited orbits may not be suitable for these regions without observations. Furthermore, the uncertainties caused by the uneven sample distribution have not been validated and eliminated. Therefore, there is an urgent need to complete the following two tasks. On the one hand, the prediction accuracy in the areas without valid observations needs to be carefully validated, in both the model training process and the real comparison process. In the model training process, the previous works have selected samples randomly to test, without building a validation method specifically for the missing data areas, which can result in overestimated prediction accuracy in the missing data areas. Therefore, it is necessary to evaluate the accuracy in the areas without valid observations, in order to obtain a more objective evaluation of the SIF reconstruction accuracy. In the real comparison process, previous works have only used the coarse-resolution GOME-2 product with a spatial resolution of 0.5°, with which it is difficult to prove the reliability of the spatial details in the reconstruction results. However, the TROPOMI instrument with a spatial resolution of 0.05° can provide ideal true data as the validation product, to assess the spatial and temporal variation of the reconstructed OCO-2 data. On the other hand, a new approach is urgently needed to meet the needs of improving the reconstruction accuracy and data availability in the areas without valid observations. The previous works have attempted to improve the prediction accuracy based on the overall samples; however, none of them have considered prediction accuracy improvement in the missing data areas as the focus. It is, therefore, necessary to make full use of the limited samples and further explore the relationship between the observations, as the swath-distributed sparse OCO-2 SIF retrievals are the only data that can be used as a reference.

In this article, in order to address the abovementioned issues, we present a new spatial and temporal constrained data-driven method to reconstruct the OCO-2 SIF product, considering the spatial and temporal characteristics of the data. The aims of this study were: 1) to develop a spatiotemporal constrained machine learning method to reconstruct OCO-2 SIF with a high degree of accuracy while considering the spatial and temporal characteristics of the data; 2) to evaluate the reconstruction uncertainties in the areas without valid observations; and 3) to compare the performance of different remote sensing inputs and machine learning models and generate a superior global contiguous 0.05°, eight-day gridded SIF product.

## II. METHOD

In this study, the light gradient boosting machine (Light-GBM) framework was chosen as the main learning model to reconstruct the OCO-2 SIF data. A spatiotemporal constrained Light-GBM model (ST-LGBM) was further developed by designing two spatial and temporal mechanism factors to further utilize the spatial and temporal correlation of the

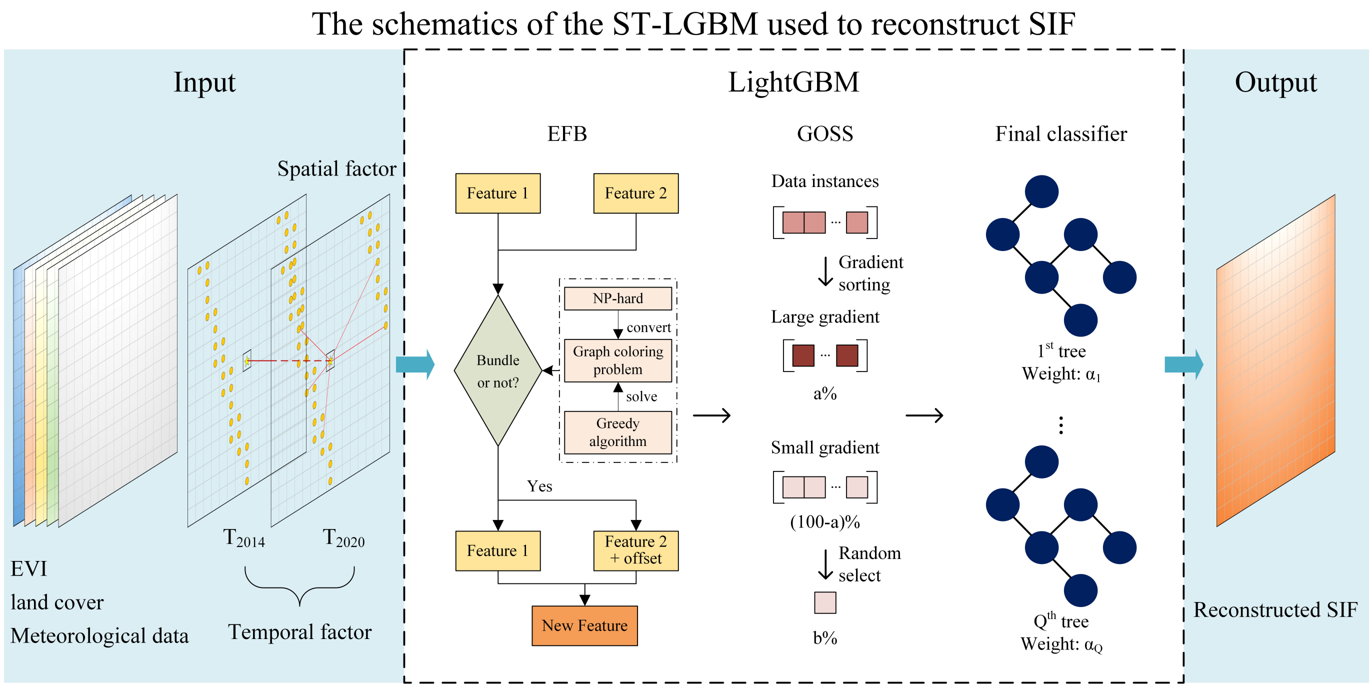

Fig. 1. Schematics of the ST-LGBM model used to reconstruct the SIF data.

swath-distributed samples. The overall framework of the proposed ST-LGBM model is shown in Fig. 1.

### *A. LightGBM Model*

Machine learning algorithms have been widely used in the SIF product generation and have been used to downscale low-resolution GOME-2 data into high-resolution data [31], [32], [33] and to reconstruct discrete OCO-2 data into continuous data [24], [25], [26]. The LightGBM model [34], which is a relatively new and efficient tree model, was selected to reconstruct the OCO-2 SIF data in this study. The LightGBM model was developed based on XGBoost [35], which is an implementation of the gradient boosting decision tree (GBDT) algorithm [36], using $K$ additive functions to predict the output. For a given input dataset with $n$ data instances, the predicted output of the $i$th instance is expressed as

$$\hat{y}_i = \phi(\boldsymbol{x}_i) = \sum_{k=1}^{K} f_k(\boldsymbol{x}_i), \quad f_k \in F \tag{1}$$

where $\boldsymbol{x}_i$ is the data instance, $F$ is the function space of the regression trees, and each $f_k$ is an independent regression tree. The objective function of the LightGBM model is

$$L(\phi) = \sum_i l(\hat{y}_i, y_i) + \sum_k \Omega(f_k) \tag{2}$$

where $l$ is the loss function, adopting the root-mean-square error (RMSE) in this case; $y_i$ is the target value; and $\Omega(f)$ is the regularization term, which is expressed as

$$\Omega(f) = \gamma T + \frac{1}{2}\lambda \|w\|^2 \tag{3}$$

where $T$ is the number of leaf nodes and $w$ is the leaf weights, which are calculated by summing the score of all the leaves. The process of minimizing the objective function uses the second-order approximation, which can quickly optimize the objective function

$$\begin{aligned} L^{(t)} &= \sum_{i=1}^{n} l(y_i, \hat{y}^{(t-1)} + f_t(\mathbf{x_i})) + \Omega(f_t) \\ &\simeq \sum_{i=1}^{n} \left[ l(y_i, \hat{y}^{(t-1)}) + g_i f_t(\mathbf{x_i}) + \frac{1}{2} h_i f_t^2(\mathbf{x_i}) \right] + \Omega(f_t) \end{aligned} \tag{4}$$

where

$$g_i = \partial_{\hat{y}^{(t-1)}} l\left(y_i, \hat{y}^{(t-1)}\right) \tag{5}$$

$$h_i = \partial^2_{\hat{y}^{(t-1)}} l\left(y_i, \hat{y}^{(t-1)}\right) \tag{6}$$

representing the first- and second-order gradients on the loss function, respectively. The LightGBM model shares the same analytical solution to the objective function as XGBoost but differs from XGBoost in terms of the split finding algorithm and tree growth strategy, adopting a histogram-based algorithm and a leafwise strategy.

The LightGBM model improves the efficiency of XGBoost through two key techniques: mutually exclusive feature bundling (EFB) and gradient-based one-side sampling (GOSS), as shown in Fig. 1. The EFB bundles mutually reduce the number of features utilizing the sparsity of the high-dimensional data, by computing the minimum sum of the nondeterministic polynomial (NP). However, this process requires completing all possible NP cases with a huge calculation, which is called an NP-hard problem [37]. In order to solve this problem, EFB converts the problem of determining what to bundle into a graph coloring problem and uses a greedy algorithm to solve it. It then adds offsets to the original features, which can be bundled to ensure that the new features can be identified. It can avoid unnecessary computation for zero feature values, so it takes up very little memory. The GOSS filters the data instances according to the data gradient, to reduce the size of the input samples. It first selects a specific proportion (i.e., $a \times 100\%$) of the top data instances sorted by the absolute value of the gradient and then randomly selects $b \times 100\%$ in the rest of the data instances and assigns a $(100 - a)/b \times 100\%$ weight to each instance. The GOSS can strike a great balance between accuracy and efficiency by reducing the samples with a small gradient, without changing the data distribution. Due to the high fitting speed, low memory usage, and optimized accuracy, the LightGBM model has been widely used in classification and prediction problems in many fields, even though it has not been open source for a long time [38].

The previous studies based on machine learning algorithms attempted to link the discrete [24], [25], [26] data to be processed with the continuous explanatory variables for the model training and then applied the trained model to generate a global product. In this case, the relationship between the discrete SIF and explanatory variables is learned using the LightGBM model and is finally applied to the continuous explanatory variables to obtain the continuous SIF data. According to the basic idea, the relationship is established as

$$\mathrm{SIF} = f(\mathrm{NIRv}, \mathrm{VPD}, \mathrm{AT}, \mathrm{PAR}, \mathrm{Landc}) \tag{7}$$

where SIF is the original OCO-2 SIF. NIRv, VPD, AT, PAR, and Landc are the explanatory variables, representing the near-infrared vegetation index (NIRv), vapor pressure deficit (VPD), air temperature (AT), photosynthetic active radiation (PAR), and land cover for convenience, respectively. Among the variables, SIF is discrete, and NIRv, VPD, AT, PAR, and Landc are all continuous. Among them, NIRv approximates the reflected proportion by vegetation at the NIR band [39], which indicates the canopy structure and plays an important role in satellite SIF [40], [41].

### B. Improved ST-LGBM Model

The methods based on the LightGBM model can only learn the relationship between the pairwise OCO-2 samples and explanatory data in the same time and space. However, the information from other OCO-2 samples in the spatial and temporal neighborhoods can also provide a core reference for the reconstruction, which is ignored in the LightGBM model. Specifically, in this case, an ST-LGBM is proposed to better use the information from the OCO-2 data in the spatial and temporal neighborhoods. In this situation, two spatial and temporal factors, considering the uneven distribution of the data samples, are designed and input into the LightGBM model as constraints, which are referred to as SIFs and SIFt. The spatiotemporal factors are calculated based on the OCO-2 original observations to further utilize the information from the swath-distributed samples, improve the reconstruction accuracy in the missing data areas, and input into the model as two additional explanatory variables. Rather than simply using inverse distance weighting used in previous studies [42], which have already improved the accuracy in atmospheric contamination [43], [44], hydrological [45], [46], climate forecast [47], [48], [49], [50], similar pixels, and vegetation phenology are introduced to further improve the spatiotemporal factors.

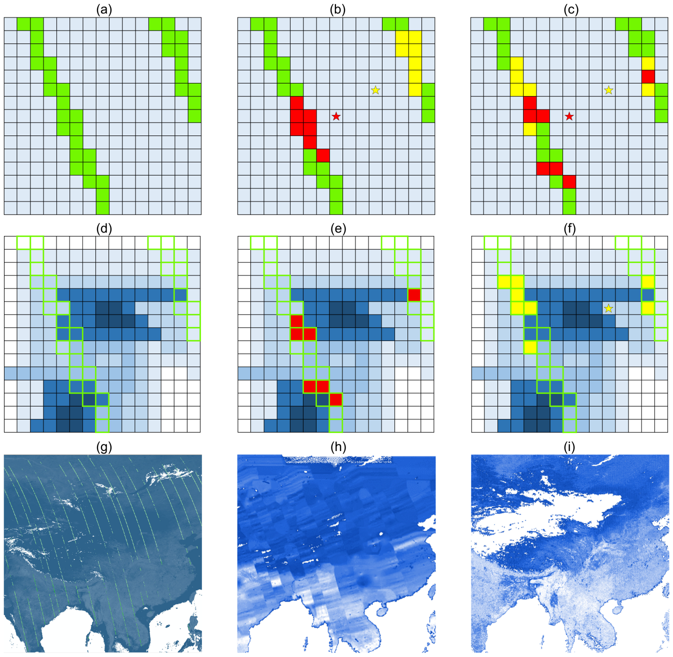

Fig. 2. Schematic of spatial factor extraction: (a), (d), and (g) distribution of SIF and NIRv, where the green pixels or swaths represent the SIF observations and the blue color in (d)–(g) represents the NIRv; (b) similar pixels only selected by distance for two target pixel marked as stars in red and yellow and (h) corresponding spatial factor is shown; (c) similar pixels selected by our method; (e) and (f) selected pixels are shown for the two target pixels; and (i) spatial factor result.

Since the original observations of OCO-2 are distributed in swaths, the nearest pixels selected solely based on the geographical distance [51] are always distributed in the same swath, as shown in Fig. 2(b). However, this may limit the reconstruction accuracy because the information from other swaths is not considered. An obvious dividing line, as shown in Fig. 2(h), may occur between two swaths in the mapping results because they use different swath pixels. In order to solve the above problems, we propose the idea of similar pixels and use the solid linear correlation between the SIF signal and the NIRv to extract the spatial factor. Since the NIRv is highly correlated with the SIF [52], the NIRv difference can be used to represent the similarity of the SIF. As a result, we sort the nearby pixels of the target pixel in adaptive window size, with an initial window size of $20 \times 20$, and then increased by 20 and limited to $90 \times 90$. The 30 pixels with the smallest NIRv differences are selected as similar pixels. Thus, the selected similar pixels should show the greatest similarity to the target pixels, compared to those with the shortest distance, and they should distribute in different swaths, as shown in Fig. 2(c). In this way, the dividing line in the calculated spatial factors also disappears, as shown in Fig. 2(i). In order to more reasonably use the information of these similar pixels, the spatial factor of the target point is calculated by the weighted sum of these similar pixels, based on the NIRv difference and

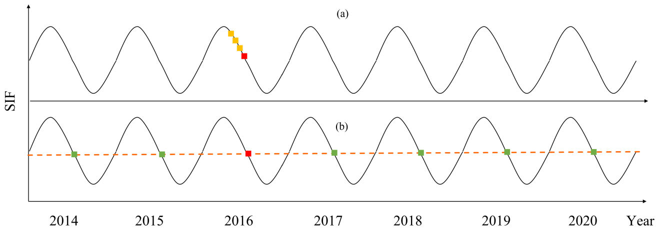

Fig. 3. Schematic of temporal factor extraction: the red points represent the target point, the yellow points in (a) represent the selected points in previous work, and the green points in (b) represent the selected points based on the vegetation phenology.

the geographic distance, according to the following equation:

$$\mathrm{SIFs} = \frac{\sum_{i=1}^{N} ws_i \times w\Delta\mathrm{NIRv}_i \times \mathrm{SIF}_i \times m}{\sum_{i=1}^{N} ws_i \times w\Delta\mathrm{NIRv}_i \times m} \tag{8}$$

where $i$ refers to the serial number of the similar points; $N$ refers to the sum of the selected similar pixels, which in this case is 30; $ws$ refers to the weight of the distance; $w\Delta\mathrm{NIRv}$ refers to the weight of the NIRv difference; SIF is the aggregated OCO-2 SIF observation; and $m$ is the number of the observations in the $i$th pixel

$$ws_i = \frac{1}{\mathrm{ds}_i^2} \tag{9}$$

where ds refers to the spatial distance.

$$w\Delta\mathrm{NIRv}_i = \frac{1}{d\Delta\mathrm{NIRv}_i} \tag{10}$$

where $w\Delta\mathrm{NIRv}$ refers to the NIRv difference.

The temporal factor is calculated based on the concept that the information from the nearby time can act as a significant reference for the target time [53]. Unlike the previous study [42] that calculated the temporal factor using the data from the prior days [as shown in Fig. 3(a)], we further revised this by considering the phenological changes and seasonal similarity in vegetation, which has been successfully used in the field of vegetation index reconstruction to achieve better results [54], [55]. Due to the phenological vegetation growth, the vegetation growth in the nearby time phases could be quite different from that in the target time. In contrast, the information from the same season of different years can provide valid information, because of the similar growth status. Based on this, we consider the phenological characteristics of vegetation to extract the temporal factor, as shown in Fig. 3(b). The temporal factor is extracted using the spatial factor in the same vegetation growth period from all the years of available OCO-2 SIF retrievals, which is expressed as follows:

$$\begin{aligned}\mathrm{SIFt}_{j,\mathrm{year}_n} &\\ = \frac{\sum_{m=1}^{n-1} \mathrm{SIFs}_{j,\mathrm{year}_m} \times wt_m + \sum_{m=n+1}^{N} \mathrm{SIFs}_{j,\mathrm{year}_m} \times wt_m}{\sum_{m=1}^{n-1} wt_m + \sum_{m=n+1}^{N} wt_m}&\end{aligned} \tag{11}$$

where $j$ refers to the point number; $\mathrm{year}_n$ is the current year; $\mathrm{year}_m$ is one of the remaining years used as a reference; $N$ refers to the total number of reference years, which is 7 in this case, i.e., from 2014 to 2020; $\mathrm{SIFs}_{j,\mathrm{year}_m}$ refers to the SIFs value of point $j$ in $\mathrm{year}_m$; and $wt_m$ is the weight of the SIFs, which is calculated by

$$wt_m = \frac{1}{\left(\mathrm{year}_m - \mathrm{year}_n\right)^2}. \tag{12}$$

The schematics of the ST-LGBM model are presented in Fig. 1. The relationship that we expect to learn is improved as

$$\mathrm{SIF} = f(\mathrm{NIRv}, \mathrm{VPD}, \mathrm{AT}, \mathrm{PAR}, \mathrm{Landc}, \mathrm{SIFs}, \mathrm{SIFt}) \tag{13}$$

where SIFs and SIFt are the spatial and temporal factors constraining the training process, respectively, and the other variables are the same as those in (7). The nulls in the spatiotemporal factors are filled using the temporal filtering method.

In addition to the LightGBM model, a deep belief network (DBN), artificial neural network (ANN), and a cubist regression tree, which are from three different machine learning method types, were also used to prove the applicability of the spatial and temporal constraints in the experiments conducted in this study.

## III. DATA FOR EXPERIMENT

### *A. OCO-2 SIF Data*

The daily-corrected SIF data (V10r) were obtained from the NASA Goddard Earth Science Data and Information Services Center [12] (https://disk.gsfc.nasa.gov/datasets/). Data from 2015 to 2018 were used in the model training process, and data from September 2014 to December 2019 were reconstructed to produce the spatiotemporally continuous product. It can be found that the sample is dense at low latitudes and sparse at high latitudes, with a larger coverage in 2015 as shown in Fig. S1 (see the Supplementary Material). Only the daily-corrected SIF retrieval at 757 nm was used in this study because it has been shown that SIF at 757 nm has a higher correlation with EC GPP and thus has greater potential in carbon cycle-related applications [56]. Only the nadir mode was used among the three provided observation modes (nadir, target, and glint) since the viewing zenith angle (VZA) for the nadir mode is close to 0° but varies for the glint and target modes in both time and space [57].

The new version OCO-2 SIF data (V10r) was applied in this study, which superseded the older version (V8r) in November 2020. The new version has added two more data filter fields and improved the bias/offset correction by selecting barren surfaces, based on a more scientific method [58], ensuring the data quality and simplifying the data filter process. Only the retrievals with the quality flag equal to 0 and nadir as the observation mode were selected and aggregated to 0.05° × 0.05° grid cells conducted when there were more than five footprints for each eight-day period. For all the pixels, the aggregation was 0.05° × 0.05° grid, to minimize the uncertainty, according to the suggestion of Frankenberg *et al.* [12].

### *B. Explanatory Variable Selection*

Five variables were selected as explanatory variables, based on photosynthetic intensity determinants and the previous works [24], [25], [26], [56], [59], which can be divided into meteorological data and remote sensing data. The meteorological data were the PAR, VPD, and AT. All the data were obtained from the ModernEra Retrospective Analysis for Research and Applications, version 2 (MERRA-2, daily, 0.5° × 0.625°) reanalysis data. These meteorological data were first resampled into 0.05° × 0.05° and then aggregated to an eight-day scale before training, in order to keep the same resolution as the target SIF product.

The remote sensing products were land cover and NIRv data. The land-cover product was the Moderate Resolution Imaging Spectroradiometer (MODIS) Land Cover Type product (MCD12C1, annual, 0.05°), which is referred to here as Landc for convenience. The NIRv data were extracted from the MODIS bidirectional reflectance distribution function (BRDF)-corrected reflectance product (MCD43C4 daily, 0.05°). The process of extracting the eight-day NIRv was calculating the daily NIRv based on (14) [60] and then aggregating the daily NIRv into an eight-day scale through the maximum synthesis method

$$\mathrm{NIRv} = \rho_{\mathrm{NIR}} \cdot \frac{\rho_{\mathrm{NIR}} - \rho_{\mathrm{RED}}}{\rho_{\mathrm{NIR}} + \rho_{\mathrm{RED}}} \tag{14}$$

where $\rho_{\mathrm{NIR}}$ represents the near-infrared reflectance and $\rho_{\mathrm{RED}}$ represents the red reflectance. In addition, the seven original MODIS reflectance bands, together with the three other most widely used vegetation indices—the normalized difference vegetation index (NDVI), enhanced vegetation index (EVI), and the leaf area index (LAI)—were also obtained as remote sensing drove data for comparison. The LAI product (eight days, 0.05°) was obtained from the National Earth System Science Data Sharing Infrastructure of China (http://www.geodata.cn). The other vegetation indices were all derived and calculated from the MCD43C4 product, using the same aggregation method that was used for the EVI.

### *C. Validation Data*

To verify the accuracy of the reconstruction processes, we compared the reconstruction results with the SIF product from TROPOMI. The TROPOMI SIF product, which is only available after 2018, is spatially continuous, with a relatively fine resolution. We used the TROPOMI SIF product produced by Köhler *et al.* [13] (ftp://fluo.gps.caltech.edu/data/tropomi/), which is ungridded retrievals at 740 nm. The data are filtered with the thresholds of 0.8 for cloud fraction, 60° for view zenith angle, 70° for solar zenith angle, and 120° for phase angle, and the grids are averaged from more than five soundings. In this study, the data from the TROPOMI product in 2018 were used to validate the consistency and distribution of the reconstructed product. Comparisons were conducted using both the eight-day data and the annual synthesis data.

## IV. EXPERIMENT AND RESULTS

### *A. Simulated Evaluation Results*

Simulated experiments were carried out by separating the OCO-2 SIF observations into a training set and a test set, using different ways to separate the two kinds of datasets.

TABLE I

VALIDATION RESULTS ON THE RANDOMLY SELECTED SAMPLES FOR THE LIGHTGBM AND ST-LGBM MODELS

| | **LightGBM** | | | | **ST-LGBM** | | | |
|---|---|---|---|---|---|---|---|---|
| | **Training set** | | **Test set** | | **Training set** | | **Test set** | |
| | **R²** | **RMSE[a]** | **R²** | **RMSE[a]** | **R²** | **RMSE[a]** | **R²** | **RMSE[a]** |
| **2015** | 0.82 | 0.07 | 0.81 | 0.07 | 0.84 | 0.06 | 0.83 | 0.07 |
| **2016** | 0.82 | 0.07 | 0.81 | 0.07 | 0.84 | 0.06 | 0.83 | 0.07 |
| **2017** | 0.82 | 0.07 | 0.81 | 0.07 | 0.84 | 0.06 | 0.82 | 0.07 |
| **2018** | 0.82 | 0.07 | 0.81 | 0.07 | 0.84 | 0.06 | 0.83 | 0.07 |
| **average** | 0.82 | 0.07 | 0.81 | 0.07 | 0.84 | 0.06 | 0.83 | 0.07 |

*a: the unit is* $Wm^{-2}\mu m^{-1}sr^{-1}$

*1) Validation on the Randomly Selected Samples:* The ten-fold cross-validation technique is applied to validate the model performance on randomly selected samples [61], i.e., randomly selecting 10% of the samples as the test set, with the others as the training set, and the average accuracy of the ten loops was calculated. The results show that the ST-LGBM model can increase prediction accuracy. As presented in Table I, the accuracy of the LightGBM model results is 0.82 for the training set and 0.81 for the test set, with an RMSE of 0.07 $\mathrm{W} \cdot \mathrm{m}^{-2} \cdot \mu\mathrm{m}^{-1} \cdot \mathrm{sr}^{-1}$. When adopting the ST-LGBM method, the prediction statistics are $R^2$ for the training set (0.84) and test set (0.83) and the RMSE for the training set (0.06 $\mathrm{W} \cdot \mathrm{m}^{-2} \cdot \mu\mathrm{m}^{-1} \cdot \mathrm{sr}^{-1}$) and test set (0.07 $\mathrm{W} \cdot \mathrm{m}^{-2} \cdot \mu\mathrm{m}^{-1} \cdot \mathrm{sr}^{-1}$). The accuracy of the training and test set evenly increases by 0.02, while the RMSE of the training set also decreases by 0.01 $\mathrm{W} \cdot \mathrm{m}^{-2} \cdot \mu\mathrm{m}^{-1} \cdot \mathrm{sr}^{-1}$ after adding the spatiotemporal factors. Fig. 4 shows the scatter plots of the test set based on all of the data for 2015–2018 as the sample. Overall, the ST-LGBM model improves the prediction accuracy, in both the quantity validation and scatter distribution. $R^2$ between the predicted SIF and observed SIF increases from 0.81 to 0.83 after adding the spatial and temporal constraints, with the same improvement in the regression slope, and the intercept also decreased by 0.01. The prediction results perform better in the high-/low-value part with a wider value range when adopting the ST-LGBM method, with fewer samples having a large range of observed value and prediction value close to zero. It is also apparent that the scatter plot between the predicted SIF and observed SIF is closer to the regression line after adding the spatiotemporal factors.

*2) Validation on the Region Without Training Samples:* The validation on the randomly selected samples can only evaluate the model's predictive ability, whereas the extrapolation problems and uncertainties caused by the uneven sample distribution cannot be evaluated. Based on this, validation on the region without training samples, which is aimed at testing the model performance on the samples out of the training sample space, is conducted according to the idea of randomly selecting some swaths as the test set and using the other swaths as the training set. As shown in Fig. 5, the global scope was divided into 23 regions to extract swaths for

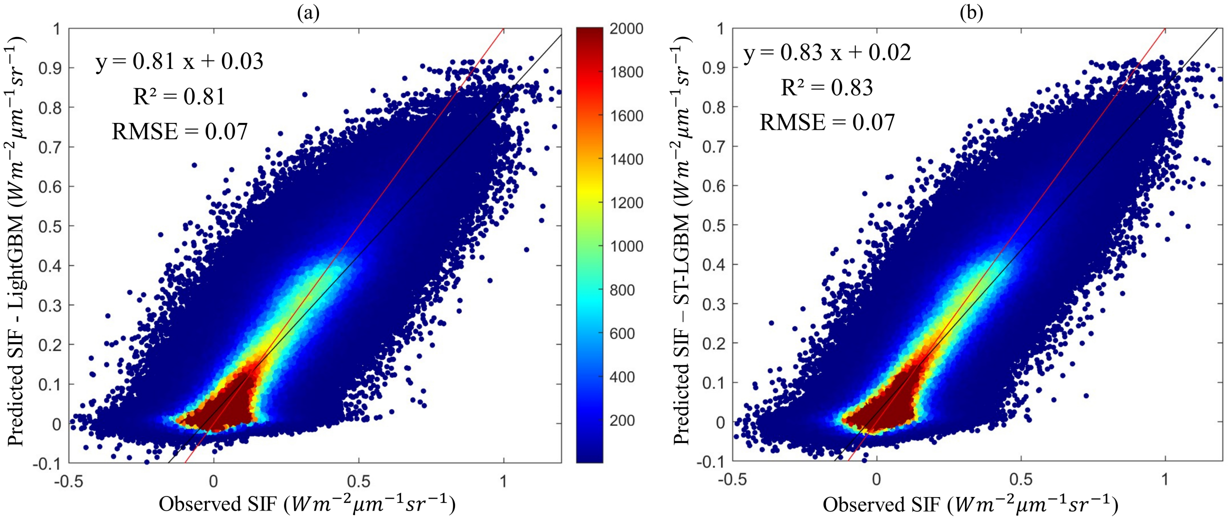

Fig. 4. Scatter plots of the validation results based on the randomly selected samples: (a) LightGBM and (b) ST-LGBM. The red line is the 1:1 line, and the black line is the regression line.

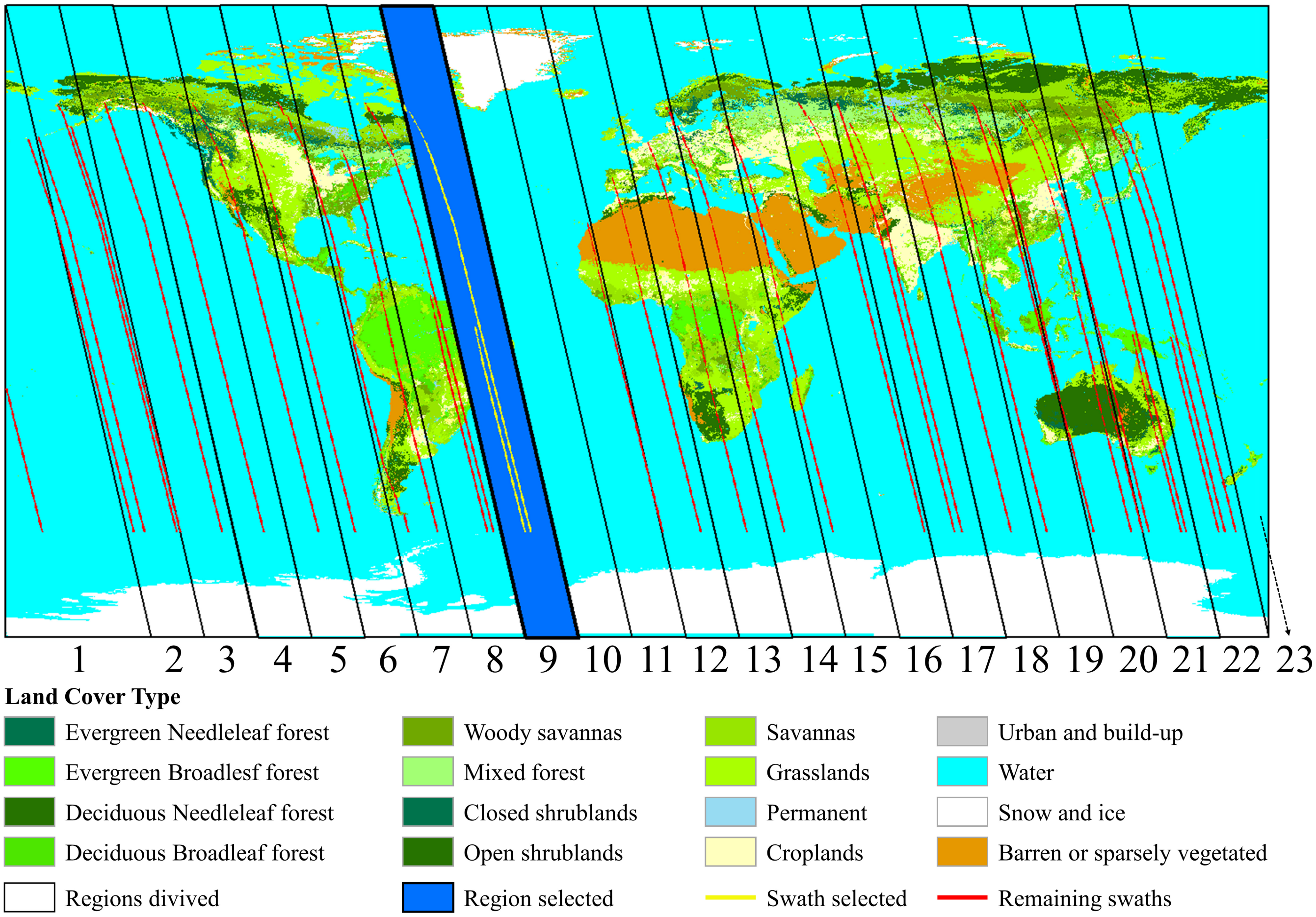

Fig. 5. Distribution of the globally divided regions. The strips are the OCO-2 data for 2015137, and the background is the land-cover type in 2015. The parallelograms filled with null values represent the divided regions, and the parallelograms filled with dark blue represent the selected region for testing. The yellow swaths are the swaths selected for testing by the selected region, while the red ones are the remaining swaths.

validation on the region without training samples, according to the mean distance between two adjacent swaths, which can form a region similar to the size of the data gaps without valid observations. The division of the regions is beneficial

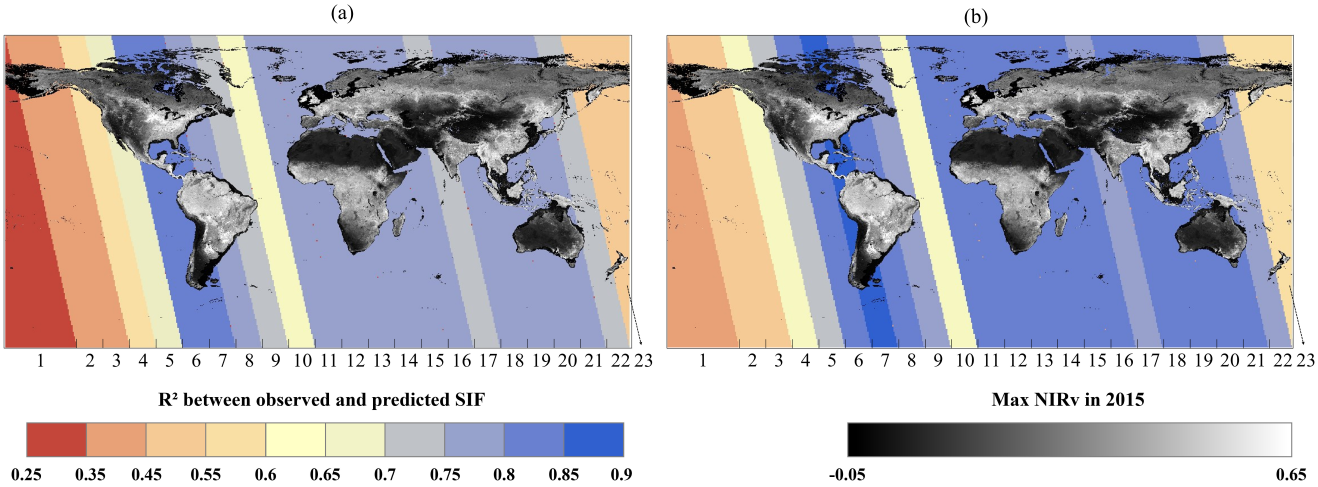

Fig. 6. $R^2$ between the observed and predicted SIF for (a) LightGBM model and (b) ST-LGBM model. The background is the max NIRv in 2015.

TABLE II

VALIDATION RESULTS ON THE REGIONS WITHOUT TRAINING SAMPLES FOR THE LIGHTGBM AND ST-LGBM MODELS

| | LightGBM | | | | ST-LGBM | | | |
|---|---|---|---|---|---|---|---|---|
| | Training set | | Test set | | Training set | | Test set | |
| | $R^2$ | RMSE[a] | $R^2$ | RMSE[a] | $R^2$ | RMSE[a] | $R^2$ | RMSE[a] |
| **2015** | 0.83 | 0.07 | 0.69 | 0.08 | 0.83 | 0.07 | 0.74 | 0.08 |
| **2016** | 0.82 | 0.07 | 0.76 | 0.08 | 0.83 | 0.07 | 0.80 | 0.07 |
| **2017** | 0.82 | 0.07 | 0.76 | 0.08 | 0.83 | 0.07 | 0.80 | 0.07 |
| **2018** | 0.82 | 0.07 | 0.75 | 0.08 | 0.83 | 0.07 | 0.80 | 0.07 |
| **average** | 0.82 | 0.07 | 0.74 | 0.08 | 0.83 | 0.07 | 0.79 | 0.07 |

*a: the unit is* $Wm^{-2}\mu m^{-1}sr^{-1}$

to the batch operation of multiscene images by reducing the manual correction process and can equalize the sample sizes of the training and test sets. The 2015057 data were selected to represent the average number of swaths, and the background was the land-cover type in 2015. All the swaths in the specific region (shown as the dark blue region) were selected as the test set (shown as the yellow swaths), and the other swaths made up the training set (shown as the red swaths), to simulate the test set ability in the areas without valid observations.

The results show that the accuracy is significantly decreased in the areas without valid observations, while the spatial and temporal constraints can clearly improve the predictive ability of the model and reduce the uncertainty in the areas without valid observations. As shown in Tables I and II, although the training accuracy of the validation on the region without training samples is similar to that of the validation on the randomly selected samples, a significant decline can be observed in the accuracy of the test set in the validation on the region without training samples in all four years when using the LightGBM model. $R^2$ for the test set decreases from 0.81 to 0.74, which is a difference of 0.07. At the same time, when using the ST-LGBM model, $R^2$ for the test set only decreases by 0.04 when compared with the validation results on the randomly selected samples, from 0.83 to 0.79, which is much less than the decrease in the results when using the LightGBM model. The comparison between the two validation methods indicates that the prediction accuracy is overestimated through validation on the randomly selected samples, leading to huge uncertainties in the prediction results in the areas without valid observations. In contrast, the spatiotemporal constraints imposed on the LightGBM model (i.e., the spatial and temporal factors) can reduce the prediction uncertainty in the missing data areas. According to Table II, when comparing the average accuracy of the validation on the region without training samples, $R^2$ increases from 0.82 to 0.83 in the training set and from 0.74 to 0.79 in the test set after adding the spatiotemporal constraints. The accuracy for the test set is improved by 0.05, which is much more than 0.01 for the training set, indicating that the spatiotemporal constraints can reduce the uncertainty in the areas without valid observations.

Swaths in every region were successively selected as the test set for validation through the validation on the region without training samples. $R^2$ for the test set was calculated and is displayed in the region position in Fig. 6, taking 0.1/0.05 as the grading of the layered coloring, with the max NIRv distribution in 2015 as the background. The results show that the prediction accuracy in areas with small sample size improves significantly when using the ST-LGBM model. Fig. 6(a) shows the distribution of $R^2$ when using the LightGBM model, which ranges from 0.29 to 0.82. When using the LightGBM model, $R^2$ in the areas with small sample size (i.e., regions 1–4, 23) is relatively low, due to the fact that there is less related information from other swaths providing a reference in the training process. In contrast, the regions with a large sample size (i.e., regions 5–8 and 11–21) have a closer relationship with the neighborhood, so the prediction accuracy is relatively high because the other swaths on the same continent and with the same characteristics provide a reference. After adding the spatial and temporal constraints to the LightGBM model, $R^2$ for the ST-LGBM model with the test set is generally improved, i.e., every strip is improved to a greater or lesser degree, as shown in Fig. 6(b). $R^2$ improves to the range of 0.36–0.86 after adopting the ST-LGBM model,

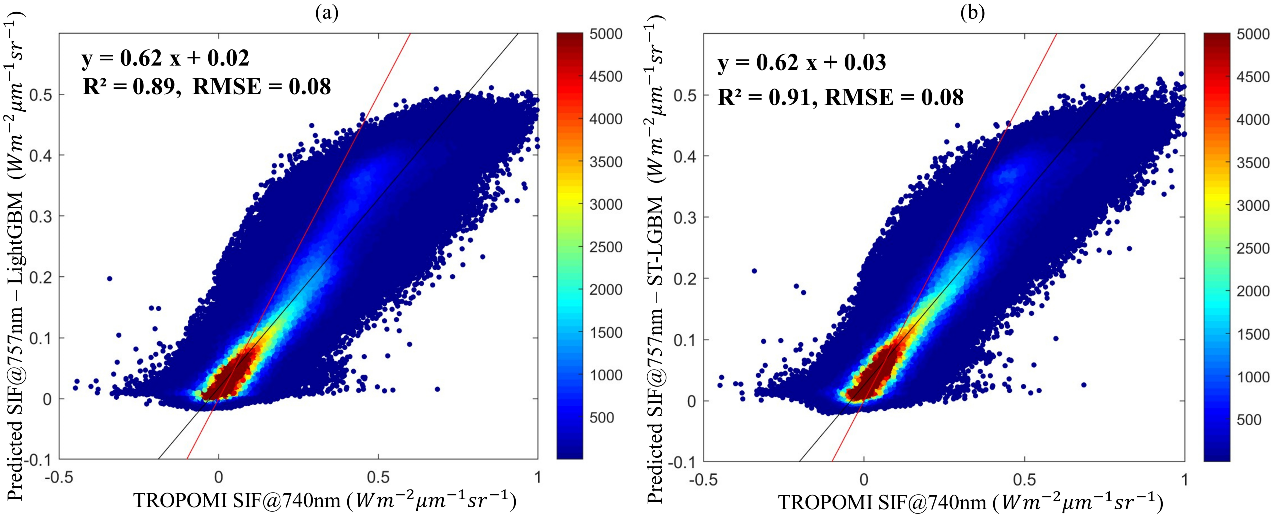

Fig. 7. Comparison between the annual average data from the TROPOMI SIF product and the predicted SIF obtained using the LightGBM (a) and ST-LGBM (b) models. The black line represents the regression line, and the red line represents the 1:1 line in the scatter plot.

with a maximum difference of 0.08 and an average of 0.05. In summary, it can be concluded that the spatial and temporal constraints reduce the uncertainties and solve the extrapolation problems out of the training sample space to a certain extent.

### *B. Real-Data Comparison With TROPOMI Data*

A real-data comparison was conducted based on real data from the TROPOMI SIF product, including quantitative analysis and qualitative comparison.

*1) Quantitative Comparison:* $R^2$ between the TROPOMI product and the reconstructed result was extracted for the quantitative comparison. The annual average SIF for the 2018 data was aggregated and plotted in scatter plots to reduce the error caused by sensor differences, as shown in Fig. 7, while the scatter between the original OCO-2 SIF and TROPOMI SIF is shown in Fig. S2(a), see the Supplementary Material. The results show that the ST-LGBM method can improve the spatial consistency of the reconstruction results with TROPOMI data and reduce the proportion of overestimations or underestimations of samples. Fig. 7 shows that the reconstruction results obtained using ST-LGBM are more accurate than those obtained using LightGBM in $R^2$. In Fig. 7(a), $R^2$ between the TROPOMI product and the predictions obtained using the LightGBM model is 0.89, with overestimations or underestimations when TROPOMI SIF with a large value range while predicted as zeros. In contrast, $R^2$ between the TROPOMI product and the predictions obtained using the ST-LGBM model increased to 0.91, with a more concentrated near the regression line distribution, and the number of overestimation and underestimation samples is also alleviated.

To further understand the temporal variations in spatial correlation, $R^2$ between the TROPOMI SIF product and the three kinds of OCO-2 SIF signals (i.e., the original observations and the predictions obtained using LightGBM/ST-LGBM) was calculated per scene throughout 2018, and the $R^2$ time series is shown in Fig. 8. The results show that the reconstruction product reduces the impact of the data quality and distribution and maintains or even improves the correlation between the multisource remote sensing SIF data. $R^2$ between the OCO-2 observation and TROPOMI is time-varying for the number, quality, and distribution of observations varied with time. The reconstruction process balanced the uneven amount and distribution of OCO-2 original observations so that there is a relatively high and stable correlation coefficient with TROPOMI SIF. The relatively low $R^2$ between two SIF retrievals is due to the relatively low data quality in early 2018 and the relatively fewer data samples and concentrated distribution at the end of 2018. The trends of $R^2$ between TROPOMI SIF and the reconstruction results are roughly consistent with the original OCO-2 SIF observations except for the scenes with very few valid observations such as 49 and 313, suggesting that the relationship between the two datasets does not change after the data reconstruction. There are sudden drops in the original OCO-2 observations, due to the difference in the data amount and distribution, such as the drop between days 305 and 321. Meanwhile, $R^2$ obtained with the reconstructed product is smoother than that of the original observations, especially from days 305 to 321, indicating that the reconstruction reduces the impact of sample size and distribution. In most scenes, the reconstructed result obtained using the LightGBM model has a higher consistency with the TROPOMI SIF than the OCO-2 observations, with a maximum difference of 0.36, while there are also six scenes whose $R^2$ is lower than the OCO-2 observations, with a maximum difference of 0.05. This phenomenon suggests that the reconstruction process using the LightGBM model improves the consistency between the SIF from two datasets in general, and however, there is no guarantee that the correlation between the two datasets will be maintained in all cases when using the LightGBM model. When adopting the ST-LGBM model, $R^2$ is always higher than the original OCO-2 retrieval, with an improvement of 0.13 on average and a maximum

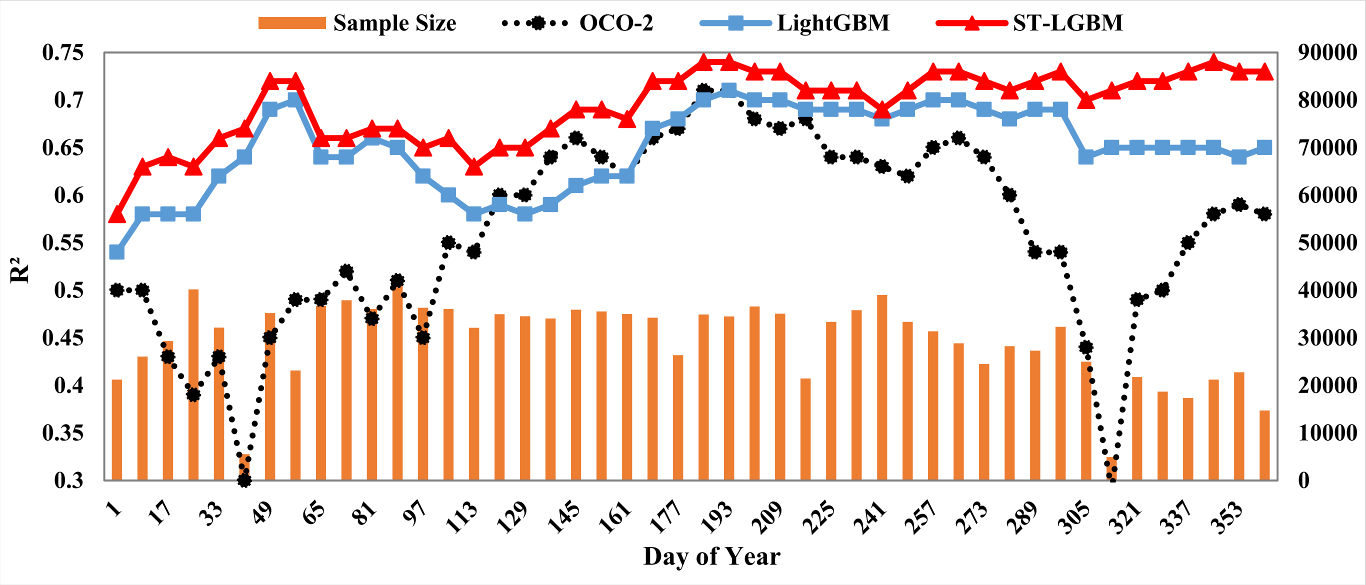

Fig. 8. $R^2$ time series between the TROPOMI SIF product and the observed SIF signal and the reconstructed SIF obtained using the LightGBM/ST-LGBM model for 2018. The orange bar chart on the subaxis represents the sample size of the original OCO-2 observations in each scene.

improvement of 0.42. This indicates that adding the spatiotemporal constraints to the LightGBM model maintains the correlation between the multisource remote sensing SIF data. Compared with the reconstructed results obtained using the LightGBM model, the ST-LGBM model improves $R^2$, with a range from 0.01 to 0.09 and an average improvement of 0.04. The main improvement is in the winter, i.e., day after 300, for there are few observations in the high latitude areas in the Northern Hemisphere, providing little reference to the model training process. While the spatiotemporal factors can get valid information from the spatiotemporal distribution of SIF data, this improves prediction accuracy. Note that the TROPOMI product is the SIF at 740 nm and the reconstructed results are the SIF at 757 nm, and the independent random error leads to the relatively low $R^2$.

$R^2$ increases in both situations after adding the spatial and temporal constraints, even though the errors have been reduced during the annual averaging process, suggesting that the ST-LGBM model steadily improves the consistency with SIF data from a different sensor.

*2) Qualitative Comparison:* For the OCO-2 SIF retrievals distributed in swaths, which provide no spatial patterns for SIF, a spatial distribution comparison of the reconstructed SIF is particularly important. The four kinds of SIF signals for 2018, i.e., predicted SIF obtained using the two models, 1° OCO-2 SIF, and TROPOMI SIF, were aggregated into the annual maximum and mean values. The comparison between the reconstructed SIF, OCO-2 original SIF, and TROPOMI SIF is shown in Figs. 9 and 10.

The spatial patterns of the four kinds of SIF products show similar distributions, but there is a significant underestimation phenomenon in the areas with a relatively high SIF value when using the LightGBM model, which is alleviated when using the ST-LGBM model. Fig. 9(1) shows that the distribution of the maximum and minimum values is roughly the same in the three global maps; however, the prediction obtained using the LightGBM model is lower than in the other three maps in the areas with a high SIF value, in many areas, especially in the Northern Hemisphere, North America, Europe, Africa, China, and Southeast Asia. Machine learning models are known to have extrapolation problems, especially for high- or low-value regions. The reconstruction results also faced extrapolation problems of Northern Russia and dryland in the west U.S. and northwest China due to the fewer samples in these areas, as shown in Fig. S1, see the Supplementary Material, while the spatiotemporal constraints can alleviate the problems, making the reconstruction SIF more similar with the original OCO-2 SIF. Three typical regions are selected and shown in Fig. 9(2)–(4), located in Europe, North America, and part of China. The three regions are all in the high latitude northern hemisphere, resulting in vegetation growth and fluorescence emission seasonally varying. The SIF value was higher in the vegetation growth season, while almost close to zero in the non-growing season. From Fig. 9(b), the reconstructed SIF obtained using the LightGBM model is faced extrapolation problems and is significantly underestimated in the three high-value regions, while the underestimation phenomenon is alleviated after adding the spatiotemporal constraints, as shown in Fig. 9(c). Compared to the two predicted products, the predicted results using ST-LGBM are generally higher in the high value of the three areas. It can be seen that the spatial patterns of reconstruction data using ST-LGBM are more similar to the TROPOMI product and the original OCO-2 SIF product than those obtained using the LightGBM model, due to the underestimation being alleviated. The underestimation using the LightGBM model can be attributed to fewer high-value samples in the sample space. Meanwhile, the spatiotemporal factors, calculated based on the real SIF observations, participate in the training process, thereby providing reference and constraints to the

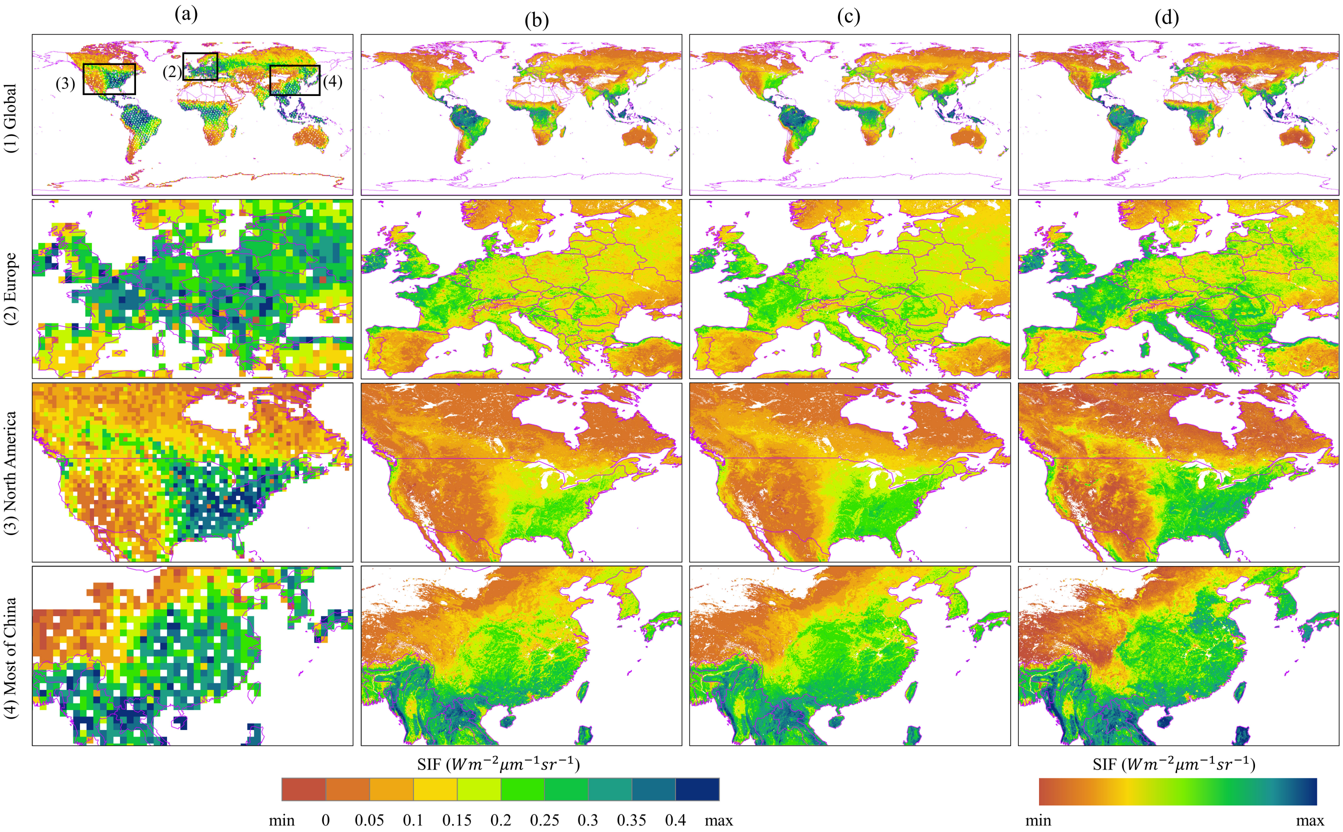

Fig. 9. Annual mean value distribution of the four types of SIF data. (a) 1° OCO-2 SIF aggregated directly. (b) Predicted SIF value pattern obtained using the LightGBM model. (c) Predicted SIF value pattern obtained using the ST-LGBM model. (d) TROPOMI SIF. Considering the different types of data, the three kinds of OCO-2 SIF signals use the same absolute hierarchical notation system, while the TROPOMI SIF displays a stretched effect to obtain a more saturated effect. Row (1) displays the global pattern, row (2) displays Europe, row (3) displays North America, and row (4) displays part of China.

TABLE III

$R^2$, RMSE, AND $R^2$ REDUCTION AFTER REMOVING ONE VARIABLE

| **Variable removed** | **R²** | | **RMSE ($Wm^{-2}\mu m^{-1}sr^{-1}$)** | | **R² reduction** | |
|---|---|---|---|---|---|---|
| | **LightGBM** | **ST-LGBM** | **LightGBM** | **ST-LGBM** | **LightGBM** | **ST-LGBM** |
| **AT** | 0.81 | 0.84 | 0.07 | 0.06 | 0.01 | 0 |
| **NIRv** | 0.60 | 0.83 | 0.10 | 0.07 | 0.22 | 0.01 |
| **Landc** | 0.81 | 0.84 | 0.07 | 0.06 | 0.01 | 0 |
| **PAR** | 0.80 | 0.84 | 0.07 | 0.07 | 0.02 | 0 |
| **VPD** | 0.81 | 0.84 | 0.07 | 0.06 | 0.01 | 0 |
| **SIFs** | / | 0.83 | / | 0.07 | / | 0.01 |
| **SIFt** | / | 0.84 | / | 0.06 | / | 0 |
| **None** | 0.82 | 0.84 | 0.07 | 0.06 | / | / |

reconstruction process. When using the ST-LGBM model, the prediction results are more similar to the spatial pattern of the TROPOMI and original OCO-2 products.

Since the mean value pattern is averaged over the whole year, the extrema will tend toward the median values. As a result, the maximum synthesis method has a stronger expressiveness for overestimation. According to Fig. 10, the same conclusion can be drawn from the annual maximum SIF distribution as the mean SIF distribution.

### *C. Sensitivity Analysis for the Explanatory Variables*

To analyze the sensitivity of the explanatory variables, we compared the accuracy of the training set when removing a certain explanatory variable. The results obtained using both models are included in the analysis. Note that, this experiment is designed only to compare the sensitivity of input data using the same method, rather than to compare the contribution of input data between different methods.

As shown in Table III, after removing a certain explanatory variable, there is a sudden drop in $R^2$ when using the LightGBM model, whereas $R^2$ stays relatively stable when any variable is removed when using the ST-LGBM model. In the reconstruction experiment using the LightGBM model, NIRv is the most sensitive explanatory variable in the five inputs. $R^2$ decreases from 0.82 to 0.60 when removing the NIRv, with a difference of 0.22, and the RMSE increases from 0.07 to 0.10 $\mathrm{W \cdot m^{-2} \cdot \mu m^{-1} \cdot sr^{-1}}$, with a difference of 0.03 $\mathrm{W \cdot m^{-2} \cdot \mu m^{-1} \cdot sr^{-1}}$. The AT, Landc, and VPD are the least sensitive of the five explanatory variables, the removal of which only reduces $R^2$ by 0.01, without changing the RMSE. The PAR also has little effect, and when removed, $R^2$ is reduced by 0.02. In comparison, the most sensitive variable is NIRv and SIFs when using the ST-LGBM model, which, when removed, decreases $R^2$ from 0.84 to 0.83, without changing the RMSE. The other variables have nearly no impact on the

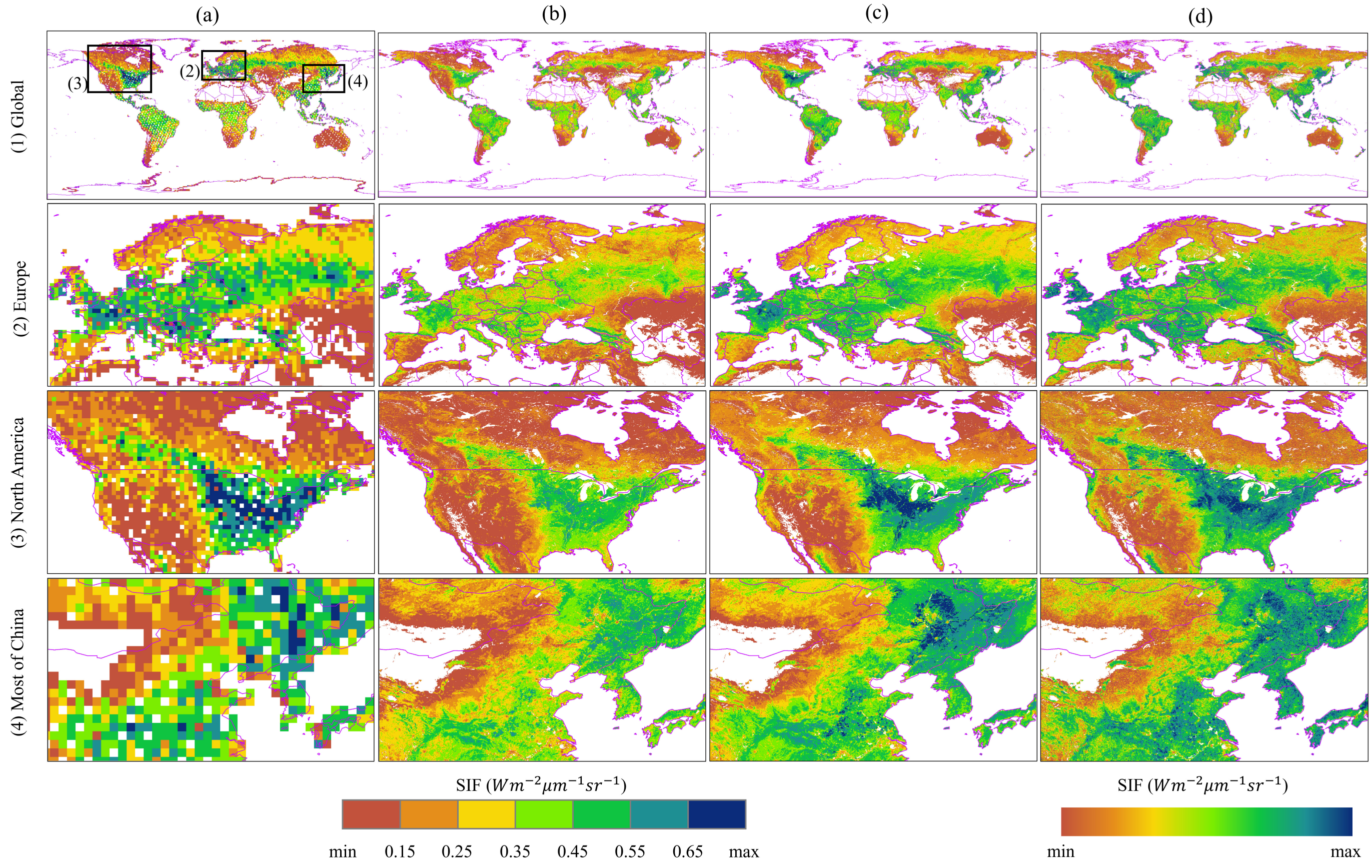

Fig. 10. Annual maximum value distribution for the four types of SIF data. (a) 1° OCO-2 SIF aggregated directly. (b) Predicted SIF value pattern obtained using the LightGBM model. (c) Predicted SIF value pattern obtained using the ST-LGBM model. (d) TROPOMI SIF. Among the different types of data, the three kinds of OCO-2 SIF signals use the same absolute hierarchical notation system, while the TROPOMI SIF displays a stretched effect in order to obtain a more saturated effect. Row (1) displays the global pattern, row (2) displays Europe, row (3) displays North America, and row (4) displays part of China.

reconstruction results, and after these variables are removed, both $R^2$ and RMSE do not change.

This indicates the spatial factor can roughly represent the information expressed by NIRv and keep the model stable even if the NIRv is missing. The spatial and temporal constraints represent the useful information from variables, reduce the variable sensitivity, improve the prediction robustness of the model, and further guarantee the prediction accuracy in the case of missing variables or noise.

### *D. Applicability Analysis*

Applicability analyses are designed to evaluate the generalizability of the proposed spatial and temporal constraints, including comparing different remote sensing inputs or machine learning models.

*1) Impacts of Different Remote Sensing Inputs:* To evaluate the applicability of the spatial and temporal constraints in different remote sensing inputs, we compared the results obtained with seven MODIS reflectance bands and four vegetation indices (i.e., EVI, NDVI, LAI, and NIRv) with the other explanatory variables (i.e., VPD, PAR, AT, and Landc) as inputs. Since validation on the region without training samples can more accurately reflect the predictive ability of the model, only validation on the region without training samples was used to compare the different inputs. Only the data from 2015 were used because the sample coverage is largest in 2015, as shown in Fig. S1 (see the Supplementary Material), and the results are similar in the four years, as mentioned above.

TABLE IV

VALIDATION RESULTS ON THE REGION WITHOUT TRAINING SAMPLES FOR DIFFERENT REMOTE SENSING INPUTS

| **Remote sensing input** | **LightGBM** | | | | **ST-LGBM** | | | |
|---|---|---|---|---|---|---|---|---|
| | **Training set** | | **Testing set** | | **Training set** | | **Testing set** | |
| | **R²** | **RMSEᵃ** | **R²** | **RMSEᵃ** | **R²** | **RMSEᵃ** | **R²** | **RMSEᵃ** |
| **Reflectance** | 0.84 | 0.07 | 0.66 | 0.08 | 0.86 | 0.06 | 0.72 | 0.07 |
| **NIRv** | 0.83 | 0.06 | 0.69 | 0.08 | 0.85 | 0.06 | 0.73 | 0.07 |
| **NDVI** | 0.80 | 0.08 | 0.63 | 0.09 | 0.85 | 0.06 | 0.72 | 0.07 |
| **LAI** | 0.75 | 0.08 | 0.53 | 0.10 | 0.85 | 0.06 | 0.71 | 0.08 |
| **EVI** | 0.84 | 0.06 | 0.68 | 0.08 | 0.86 | 0.06 | 0.72 | 0.07 |

*a: the unit is* $Wm^{-2}\mu m^{-1}sr^{-1}$

As shown in Table IV, the spatial and temporal constraints can improve the predictive ability of the reconstruction model and provide relatively stable results when using different remote sensing inputs. In addition, the NIRv performs the best in the OCO-2 SIF reconstruction task. The training set

$R^2$ of the five remote sensing input combinations is 0.84 for reflectance and EVI, 0.83 for NIRv, 0.80 for NDVI, and 0.75 for LAI, and the test set $R^2$ is 0.69 for NIRv, 0.68 for EVI, 0.66 for reflectance, 0.63 for NDVI, and 0.53 for LAI. The accuracy obtained using the LightGBM model shows a sudden drop in the missing data areas, no matter which input is selected, and the performance is EVI > NIRv > reflectance > NDVI > LAI. After adding the spatial and temporal constraints to the LightGBM model, the accuracy obtained using the ST-LGBM model shows the same trends: the $R^2$ for the training set is 0.86 for reflectance and EVI, and 0.85 for the NIRv and NDVI, and LAI, and $R^2$ for the test set is 0.73 for NIRv, 0.72 for reflectance, EVI, and NDVI, and 0.71 for LAI. The spatio-temporal constraints increase the $R^2$ for the test set by 0.04 for NIRv and EVI, 0.06 for reflectance, 0.09 for NDVI, and 0.18 for LAI. The worse the result obtained using the LightGBM model, the more improved the result is after adding the spatiotemporal constraints that the impacts of different remote sensing inputs are weakened by the spatiotemporal constraints, which agrees with the conclusion drawn in Section IV-C. Although the spatiotemporal constraints improve the performance of all the remote sensing inputs, the NIRv still obtains the best results.

A deeper comparison between EVI, NIRv, seven MODIS reflectance bands, and the NIR band is shown in Table S I (validation results based on the randomly selected samples) and Table S II (validation results on the region without training samples), see the Supplementary Material. Both EVI and NIRv are used to extract spatial and temporal factors, the NIRv-based factors are only used combined with NIRv, and the other inputs are all used with EVI-based factors. NIRv and NIRv-based spatiotemporal factors are finally selected to reconstruct SIF since the combination has the best performance for the reconstruction task in the validation on the region without training samples.

*2) Impacts of Different Machine Learning Models:* In order to further confirm the applicability of the proposed spatiotemporal constraints, we also compared the results obtained using other machine learning algorithms. Three models from three different machine learning categories (deep learning models, neural networks, and tree models) were selected for comparison, i.e., DBN, ANN, and Cubist, as shown in Table V.

Table V shows that the spatial and temporal constraints can improve the accuracy for the regions without valid observantions, and when changing the reconstruction model, the spatiotemporal constraints remain effective, but among all the models, the LightGBM model performs the best. As can be seen in Table V, in the validation on the randomly selected samples, $R^2$ for the test set is 0.79 (DBN), 0.77 (ANN), 0.80 (Cubist), and 0.82 (LightGBM). After adding the spatiotemporal constraints, $R^2$ for the test set is 0.82 (DBN), 0.81 (ANN), 0.82 (Cubist), and 0.84 (LightGBM). $R^2$ of these models is improved by 0.03 (DBN), 0.02 (Cubist), 0.04 (ANN), and 0.02 (LightGBM). In the validation on the region without training samples, $R^2$ for the test set is 0.69 for all the models, and when using the spatial and temporal constrained learning method, $R^2$ for the test set is increased to 0.73 for DBN, ANN, and Cubist, and 0.74 for LightGBM, which are improvements of 0.04 (DBN, ANN, and Cubist) and 0.05 (LightGBM). No matter which learning model is selected, the results are roughly the same: the accuracy for the missing data areas drops significantly, but the spatiotemporal constraints can alleviate the decrease. Overall, the ST-LGBM model performs the best in the OCO-2 SIF reconstruction process.

TABLE V

$R^2$ AND RMSE COMPARISON WHEN USING DIFFERENT MACHINE LEARNING MODELS IN A SIMULATED EXPERIMENT

| Model | Validation on the randomly selected samples | | | | Validation on the region without training samples | | | |
|---|---|---|---|---|---|---|---|---|
| | Training set | | Test set | | Training set | | Test set | |
| | $R^2$ | RMSE[a] | $R^2$ | RMSE[a] | $R^2$ | RMSE[a] | $R^2$ | RMSE[a] |
| **LightGBM** | 0.82 | 0.07 | 0.81 | 0.07 | 0.83 | 0.07 | 0.69 | 0.08 |
| **ST-LGBM** | 0.84 | 0.06 | 0.83 | 0.07 | 0.83 | 0.07 | 0.74 | 0.07 |
| **DBN** | 0.79 | 0.07 | 0.79 | 0.07 | 0.79 | 0.07 | 0.69 | 0.08 |
| **ST-DBN** | 0.82 | 0.07 | 0.82 | 0.07 | 0.83 | 0.07 | 0.73 | 0.07 |
| **ANN** | 0.77 | 0.08 | 0.77 | 0.08 | 0.78 | 0.07 | 0.69 | 0.08 |
| **ST-ANN** | 0.81 | 0.07 | 0.81 | 0.07 | 0.82 | 0.07 | 0.73 | 0.07 |
| **Cubist** | 0.80 | 0.07 | 0.80 | 0.07 | 0.81 | 0.07 | 0.69 | 0.08 |
| **ST-Cubist** | 0.82 | 0.07 | 0.82 | 0.07 | 0.83 | 0.07 | 0.73 | 0.07 |

*a: the unit is* $Wm^{-2}\mu m^{-1}sr^{-1}$

## V. DISCUSSION

The OCO-2 SIF retrieval has a fine footprint and can fit EC flux tower GPP well, making it one of the satellite SIF products with the most potential among the current products. Nevertheless, the spatial discontinuity (i.e., the gaps between adjacent swaths are 30 times more than the width of the swaths) limits the application of the product. Against this background, we propose a reconstruction method coupling a geoecological mechanism (i.e., spatial and temporal factors) and a machine learning model (i.e., LightGBM), to improve the reconstruction accuracy by considering the data distribution and vegetation growth cycle. The spatiotemporal constraints improve the reconstruction accuracy in the areas without valid observations (Table II and Fig. 6), reduce the model overestimation and underestimation (Figs. 7, 9, and 10), and increase the correlation with the TROPOMI SIF product in both quality (Figs. 9 and 10) and quantity (Figs. 7 and 8), without additional data input. The spatially continuous SIF product with a 0.05°, eight-day resolution covering a time series from September 2014 to December 2019 is freely available at http://rs-pop.whu.edu.cn/#/. The advantages mentioned above reduce product uncertainty and improve product applicability, leading to the product having great potential in many fields, such as agriculture, forestry, climate change, and carbon cycle studies.

There are big uncertainties in the reconstruction results obtained using the traditional machine learning methods in areas without valid observations (Table II and Fig. 6), limiting the application of the reconstructed products. The reconstruction accuracy in the missing data areas decreases significantly, as shown in the validation results on the region without training samples and the spatial distribution comparison. In the validation on the region without training samples, the regions with a small sample size have a relatively low $R^2$ because of the reduction in the related information from the other swaths of the more complex SIF signal. There is also an underestimation phenomenon in the areas with high SIF values, due to the sample distribution in the sample space and lack of geoecological mechanism constraint. In summary, the uncertainties in the missing data areas are due to the fact that the implicit relationship between the swath-distributed data is not mined and applied in the learning process so the models have relatively low portability. Therefore, a new approach is urgently needed in the reconstruction task.

The coupling of the mechanism and machine learning method has shown an advantage, due to the complementary strengths of the two processes [62]: the mechanism benefits from the relatively stable model, rigorous logic, and explicable results; and the machine learning model benefits from the high efficiency, strong expansibility, and the fact that no prior knowledge is required. The coupling of a mechanism and machine learning method has been widely used in the remote sensing field, including atmospheric [42] and hydrological [45] remote sensing. However, there have been relatively few studies of vegetation based on remote sensing, especially in the SIF product generation. Due to the convenience of the machine learning models and the complexity of the vegetation process mechanism, most of the SIF product generation studies have been based only on machine learning models [24], [25], [26], [31], [32]. Although previous works have generated an SIF product using a geoecological mechanism [63], we are not aware of any studies that have attempted to integrate a geoecological mechanism and machine learning. The spatiotemporal factors considered in this study are a preliminary attempt to combine the geoecological mechanism and machine learning, with the aim being to combine the respective advantages of the two processes, to make up for their shortcomings. The spatial factor is the average weighted by the points with the smallest NIRv difference with the target point, according to the two weights (i.e., the NIRv difference and geographical distance). The spatial factor mines the vegetation similarity information provided by the pixels with a similar vegetation index value and geographical similarity, based on Tobler's first law [51]. The temporal factor introduces the vegetation phenology, using the spatial factor over the years to calculate this, i.e., all of the spatial factors are averagely weighted using the temporal distance. The spatiotemporal factors are calculated from the SIF values of the spatial and temporal neighbors, reflecting the true level of SIF and providing the geographic and biophysical constraints for machine learning, which can improve accuracy and reduce overestimation.

Since there already are some works that tried to reconstruct the OCO-2 SIF and get continuous products, it is important to compare our results with them. Actually, the result of LightGBM in this article is exactly the training method similar to the previous studies [25], [26], and the comparison between ST-LGBM and LightGBM is a fair comparison to prove the advantage of our proposed spatial and temporal constraints that are training using the same model with and without spatial and temporal factors. A similar accuracy can also be obtained between LightGBM and previous products when compared with TROPOMI SIF (Figs. 7 and S2 see the Supplementary Material). The ST-LGBM can further improve the correlation between reconstruction SIF and TROPOMI SIF and get a product with a more detailed spatial distribution (Fig. S3, see the Supplementary Material). The direct comparison between our ST-LGBM and previous products would be impacted by many factors such as different models and inputted explanatory variables. From the literature, previous works are all only validated on the randomly selected samples with $R^2$ around 0.79, our method can improve the accuracy by about 0.04. We believe that our product can also perform much better when validating on the area without samples, just like compared with LightGBM, because combining the spatiotemporal constraints and the machine learning model can provide a reference in the areas without valid observations. When applying the reconstructed SIF product to monitor specific drought events, the results further support that the ST-LGBM can respond better to drought events than using LightGBM (Figs. S4 and S5, see the Supplementary Material), in the period with large interannual variations in the SIF value.

Further work needs to be conducted in the four following aspects. First, much could be done in the mechanism constraint construction process, such as synthesizing multisource SIF data. The mechanism constraints in this study were constructed based only on the original OCO-2 product, without considering the multisource SIF information from other datasets that are spatially continuous, such as TROPOMI or GOME-2. Second, only the effect of remote sensing data was compared in this study, and other meteorological products or parameters, such as soil moisture, evapotranspiration, or land surface temperature (LST), could be considered in the follow-up research. Third, although the reconstruction process can improve the spatial resolution of the OCO-2 SIF product from 1° to 0.05°, the resolution is still not sufficient for small-scale vegetation research. This study mainly verified the effectiveness of the approach of coupling a geoecological mechanism and machine learning so that the product was only reconstructed at the same resolution as the previous works [24], [25], [26]. Further research could attempt to reconstruct the SIF product into a finer resolution using input data with a higher resolution [33], [64], such as 1 km. Finally, many recent studies have shown that the SIF at the photosystem level should be reconstructed at the canopy level to gain a stronger correlation with GPP [65]. However, the reconstruction process in this study was the same as in the previous works [24], [25], [26], i.e., the original OCO-2 SIF retrieval was used, without correcting the canopy level. A comparison between an SIF product with or without canopy-level correction would be worthwhile. Many correction algorithms have been developed in previous research [66], which could be directly used in the reconstructed SIF product in follow-up research.

## VI. CONCLUSION

In this study, OCO-2 SIF retrievals were reconstructed using a spatial and temporal constrained LightGBM model (ST-LGBM), and a global 0.05°, eight-day resolution SIF product with high accuracy was generated. The improved spatial and temporal factors were designed to utilize the relationships from the limited data samples by introducing similar pixels and vegetation phenology, which were input into the LightGBM model as spatial and temporal constraints. Simulated experiments, including validation on the randomly selected samples and validation on the region without training samples, and a real-data comparison with the TROPOMI product, were conducted to evaluate the reconstruction accuracy. The main conclusions are given as follows.

1) The comparison between the two validation methods of simulation experiments indicated enormous uncertainty in the areas without valid SIF observations. $R^2$ was 0.82 for the training set and 0.81 for the test set when validating on the randomly selected samples, while $R^2$ for the test set dropped to 0.74 and the training set accuracy remained the same when validating on the region without training samples. The prediction accuracy in areas with a small sample size significantly decreased because there was less related information from the other swaths providing references in the training process.
2) The spatial and temporal constraints can improve the prediction accuracy, improve the robustness of the OCO-2 reconstruction results, and reduce the variable sensitivity. The ST-LGBM model reduces the influence of the data quality and distribution on the reconstruction process and solves the problem of model prediction in the missing data areas, to a certain extent. The consistency with the SIF data from a different sensor was also improved in the qualitative and quantitative comparison, by alleviating the underestimation by adopting the ST-LGBM model.
3) The sensitivity and applicability analyses showed that the spatial and temporal constraints can support relatively stable results when using various input combinations or different machine learning models. The spatial and temporal factors reduce the model sensitivity to the other inputs and can obtain stable results when using different input combinations or different machine learning models.

## ACKNOWLEDGMENT

The authors would like to thank the National Earth System Science Data Center of the National Science and Technology Infrastructure of China (http://www.geodata.cn) for the data support. They would also like to thank P. Köhler for making the high-quality TROPOspheric Monitoring Instrument (TROPOMI) datasets (ftp://fluo.gps.caltech.edu/data/tropomi/) used in this study.

## REFERENCES

[1] M. Ashraf and P. J. C. Harris, "Photosynthesis under stressful environments: An overview," *Photosynthetica*, vol. 51, no. 2, pp. 163–190, Jun. 2013.

[2] C. Beer *et al.*, "Terrestrial gross carbon dioxide uptake: Global distribution and covariation with climate," *Science*, vol. 329, no. 5993, pp. 834–838, Aug. 2010.

[3] B. K. Wylie *et al.*, "Adaptive data-driven models for estimating carbon fluxes in the Northern Great Plains," *Remote Sens. Environ.*, vol. 106, no. 4, pp. 399–413, Feb. 2007.

[4] P. J. Sellers *et al.*, "Modeling the exchanges of energy, water, and carbon between continents and the atmosphere," *Science*, vol. 275, no. 5299, pp. 502–509, Jan. 1997.

[5] S. W. Running, R. R. Nemani, F. A. Heinsch, M. Zhao, M. Reeves, and H. Hashimoto, "A continuous satellite-derived measure of global terrestrial primary production," *BioScience*, vol. 54, no. 6, p. 547, 2004.

[6] A. Anav *et al.*, "Spatiotemporal patterns of terrestrial gross primary production: A review," *Rev. Geophys.*, vol. 53, no. 3, pp. 785–818, Sep. 2015.

[7] G. H. Mohammed *et al.*, "Remote sensing of solar-induced chlorophyll fluorescence (SIF) in vegetation: 50 years of progress," *Remote Sens. Environ.*, vol. 231, Sep. 2019, Art. no. 111177.

[8] P. Wagle, Y. Zhang, C. Jin, and X. Xiao, "Comparison of solar-induced chlorophyll fluorescence, light-use efficiency, and process-based GPP models in maize," *Ecol. Appl.*, vol. 26, no. 4, pp. 1211–1222, Jun. 2016.

[9] Y. Zhang *et al.*, "On the relationship between sub-daily instantaneous and daily total gross primary production: Implications for interpreting satellite-based SIF retrievals," *Remote Sens. Environ.*, vol. 205, pp. 276–289, Feb. 2018.

[10] P. Köhler, L. Guanter, and J. Joiner, "A linear method for the retrieval of sun-induced chlorophyll fluorescence from GOME-2 and SCIAMACHY data," *Atmos. Meas. Techn.*, vol. 8, no. 6, pp. 2589–2608, Jun. 2015.

[11] J. Joiner *et al.*, "Global monitoring of terrestrial chlorophyll fluorescence from moderate-spectral-resolution near-infrared satellite measurements: Methodology, simulations, and application to GOME-2," *Atmos. Meas. Techn.*, vol. 6, no. 10, pp. 2803–2823, Oct. 2013.

[12] C. Frankenberg *et al.*, "Prospects for chlorophyll fluorescence remote sensing from the orbiting carbon observatory-2," *Remote Sens. Environ.*, vol. 147, pp. 1–12, May 2014.

[13] P. Köhler, C. Frankenberg, T. S. Magney, L. Guanter, J. Joiner, and J. Landgraf, "Global retrievals of solar-induced chlorophyll fluorescence with TROPOMI: First results and intersensor comparison to OCO-2," *Geophys. Res. Lett.*, vol. 45, no. 19, pp. 10456–10463, Oct. 2018.

[14] H. Gao *et al.*, "Global analysis of the relationship between reconstructed solar-induced chlorophyll fluorescence (SIF) and gross primary production (GPP)," *Remote Sens.*, vol. 13, no. 14, Jan. 2021, Art. no. 2824.

[15] N. C. Parazoo *et al.*, "Terrestrial gross primary production inferred from satellite fluorescence and vegetation models," *Global Change Biol.*, vol. 20, no. 10, pp. 3103–3121, Oct. 2014.

[16] L. He *et al.*, "From the ground to space: Using solar-induced chlorophyll fluorescence to estimate crop productivity," *Geophys. Res. Lett.*, vol. 47, no. 7, Apr. 2020, Art. no. e2020GL087474.

[17] X. Wei, X. Wang, W. Wei, and W. Wan, "Use of sun-induced chlorophyll fluorescence obtained by OCO-2 and GOME-2 for GPP estimates of the Heihe River Basin, China," *Remote Sens.*, vol. 10, no. 12, p. 2039, Dec. 2018.

[18] J. A. Gamon, "Reviews and syntheses: Optical sampling of the flux tower footprint," *Biogeosciences*, vol. 12, no. 14, pp. 4509–4523, Jul. 2015.

[19] Y. Sun *et al.*, "Overview of solar-induced chlorophyll fluorescence (SIF) from the orbiting carbon observatory-2: Retrieval, cross-mission comparison, and global monitoring for GPP," *Remote Sens. Environ.*, vol. 209, pp. 808–823, May 2018.

[20] J. Joiner, Y. Yoshida, A. P. Vasilkov, Y. Yoshida, L. A. Corp, and E. M. Middleton, "First observations of global and seasonal terrestrial chlorophyll fluorescence from space," *Biogeosciences*, vol. 8, no. 3, pp. 637–651, Mar. 2011.

[21] T. E. Taylor *et al.*, "OCO-3 early mission operations and initial (vEarly) $XCO_2$ and SIF retrievals," *Remote Sens. Environ.*, vol. 251, Dec. 2020, Art. no. 112032.

[22] R. R. Basilio, M. W. Bennett, A. Eldering, P. R. Lawson, and R. A. Rosenberg, "Orbiting carbon observatory-3 (OCO-3), remote sensing from the international space station (ISS)," *Proc. SPIE*, vol. 11151, pp. 42–55, Oct. 2019.

[23] G. Pan, Y. Xu, and J. Ma, "The potential of $CO_2$ satellite monitoring for climate governance: A review," *J. Environ. Manag.*, vol. 277, Jan. 2021, Art. no. 111423.

[24] L. Yu, J. Wen, C. Y. Chang, C. Frankenberg, and Y. Sun, "High-resolution global contiguous SIF of OCO-2," *Geophys. Res. Lett.*, vol. 46, no. 3, pp. 1449–1458, Feb. 2019.

[25] Y. Zhang, J. Joiner, S. H. Alemohammad, S. Zhou, and P. Gentine, "A global spatially contiguous solar-induced fluorescence (CSIF) dataset using neural networks," *Biogeosciences*, vol. 15, no. 19, pp. 5779–5800, Oct. 2018.

[26] X. Li and J. Xiao, "A global, 0.05-degree product of solar-induced chlorophyll fluorescence derived from OCO-2, MODIS, and reanalysis data," *Remote Sens.*, vol. 11, no. 5, p. 517, Mar. 2019.

[27] D. Yang, X. Xu, F. Xiao, C. Xu, W. Luo, and L. Tao, "Improving modeling of ecosystem gross primary productivity through re-optimizing temperature restrictions on photosynthesis," *Sci. Total Environ.*, vol. 788, Sep. 2021, Art. no. 147805.

[28] T. M. Wei and A. P. Barros, "Prospects for long-term agriculture in Southern Africa: Emergent dynamics of Savannah ecosystems from remote sensing observations," *Remote Sens.*, vol. 13, no. 15, p. 2954, Jul. 2021.

[29] W. Jiao, L. Wang, W. K. Smith, Q. Chang, H. Wang, and P. D'Odorico, "Observed increasing water constraint on vegetation growth over the last three decades," *Nature Commun.*, vol. 12, no. 1, p. 3777, Dec. 2021.

[30] Y. Zhang, R. Commane, S. Zhou, A. P. Williams, and P. Gentine, "Light limitation regulates the response of autumn terrestrial carbon uptake to warming," *Nature Climate Change*, vol. 10, no. 8, pp. 739–743, Aug. 2020.

[31] P. Gentine and S. H. Alemohammad, "Reconstructed solar-induced fluorescence: A machine learning vegetation product based on MODIS surface reflectance to reproduce GOME-2 solar-induced fluorescence," *Geophys. Res. Lett.*, vol. 45, no. 7, pp. 3136–3146, 2018.

[32] J. Wen *et al.*, "A framework for harmonizing multiple satellite instruments to generate a long-term global high spatial-resolution solar-induced chlorophyll fluorescence (SIF)," *Remote Sens. Environ.*, vol. 239, Mar. 2020, Art. no. 111644.

[33] Z. Zhang, W. Xu, Q. Qin, and Z. Long, "Downscaling solar-induced chlorophyll fluorescence based on convolutional neural network method to monitor agricultural drought," *IEEE Trans. Geosci. Remote Sens.*, vol. 59, no. 2, pp. 1012–1028, Feb. 2021.

[34] G. Ke *et al.*, "LightGBM: A highly efficient gradient boosting decision tree," in *Proc. Adv. Neural Inf. Process. Syst.*, 2017, p. 9.

[35] T. Chen and C. Guestrin, "XGBoost: A scalable tree boosting system," in *Proc. 22nd ACM SIGKDD Int. Conf. Knowl. Discovery Data Mining*, San Francisco, CA, USA, Aug. 2016, pp. 785–794.

[36] J. H. Friedman, "Greedy function approximation: A gradient boosting machine," *Ann. Stat.*, vol. 29, no. 5, pp. 1189–1232, Oct. 2001.

[37] A. J. Mansfield and D. J. A. Welsh, "Some colouring problems and their complexity," in *North-Holland Mathematics Studies*, vol. 62. Amsterdam, The Netherlands: Elsevier, 1982, pp. 159–170.

[38] Y. Liang *et al.*, "Product marketing prediction based on XGboost and LightGBM algorithm," in *Proc. 2nd Int. Conf. Artif. Intell. Pattern Recognit.*, New York, NY, USA, Aug. 2019, pp. 150–153.

[39] G. Badgley, L. D. L. Anderegg, J. A. Berry, and C. B. Field, "Terrestrial gross primary production: Using $\mathrm{NIR_V}$ to scale from site to globe," *Global Change Biol.*, vol. 25, no. 11, pp. 3731–3740, 2019.

[40] Y. Zeng, G. Badgley, B. Dechant, Y. Ryu, M. Chen, and J. A. Berry, "A practical approach for estimating the escape ratio of near-infrared solar-induced chlorophyll fluorescence," *Remote Sens. Environ.*, vol. 232, Oct. 2019, Art. no. 111209.

[41] P. Yang and C. van der Tol, "Linking canopy scattering of far-red sun-induced chlorophyll fluorescence with reflectance," *Remote Sens. Environ.*, vol. 209, pp. 456–467, May 2018.

[42] T. Li, H. Shen, Q. Yuan, X. Zhang, and L. Zhang, "Estimating ground-level $\mathrm{PM}_{2.5}$ by fusing satellite and station observations: A geo-intelligent deep learning approach: Deep learning for $\mathrm{PM}_{2.5}$ estimation," *Geophys. Res. Lett.*, vol. 44, no. 23, pp. 11985–11993, Dec. 2017.

[43] T. Li, H. Shen, C. Zeng, Q. Yuan, and L. Zhang, "Point-surface fusion of station measurements and satellite observations for mapping $\mathrm{PM}_{2.5}$ distribution in China: Methods and assessment," *Atmos. Environ.*, vol. 152, pp. 477–489, Mar. 2017.

[44] L. Yang, L. Shi, J. Wei, and Y. Wang, "Spatiotemporal evolution of ecological environment quality in arid areas based on the remote sensing ecological distance index: A case study of Yuyang district in Yulin city, China," *Open Geosci.*, vol. 13, no. 1, pp. 1701–1710, Jan. 2021.

[45] Z. Liang, R. Zou, X. Chen, T. Ren, H. Su, and Y. Liu, "Simulate the forecast capacity of a complicated water quality model using the long short-term memory approach," *J. Hydrol.*, vol. 581, Feb. 2020, Art. no. 124432.

[46] J. S. Read *et al.*, "Process-guided deep learning predictions of lake water temperature," *Water Resour. Res.*, vol. 55, no. 11, pp. 9173–9190, 2019.

[47] T. Beucler, S. Rasp, M. Pritchard, and P. Gentine, "Achieving conservation of energy in neural network emulators for climate modeling," Jun. 2019, *arXiv:1906.06622*.

[48] R. Cintra, H. de Campos Velho, and S. Cocke, "Tracking the model: Data assimilation by artificial neural network," in *Proc. Int. Joint Conf. Neural Netw. (IJCNN)*, Jul. 2016, pp. 403–410.

[49] J. Lu, W. Hu, and X. Zhang, "Precipitation data assimilation system based on a neural network and case-based reasoning system," *Information*, vol. 9, no. 5, May 2018, Art. no. 106.

[50] M. Bonavita and P. Laloyaux, "Machine learning for model error inference and correction," *J. Adv. Model. Earth Syst.*, vol. 12, no. 12, 2020, Art. no. e2020MS002232.

[51] W. R. Tobler, "A computer movie simulating urban growth in the Detroit region," *Econ. Geogr.*, vol. 46, pp. 234–240, Jun. 1970.

[52] B. Dechant *et al.*, "NIRVP: A robust structural proxy for sun-induced chlorophyll fluorescence and photosynthesis across scales," *Remote Sens. Environ.*, vol. 268, Jan. 2022, Art. no. 112763.

[53] Q. Yuan, L. Zhang, and H. Shen, "Hyperspectral image denoising employing a spectral–spatial adaptive total variation model," *IEEE Trans. Geosci. Remote Sens.*, vol. 50, no. 10, pp. 3660–3677, Oct. 2012.

[54] D. Chu *et al.*, "Long time-series NDVI reconstruction in cloud-prone regions via spatio-temporal tensor completion," *Remote Sens. Environ.*, vol. 264, Oct. 2021, Art. no. 112632.

[55] C. Ruyin *et al.*, "A simple method to improve the quality of NDVI time-series data by integrating spatiotemporal information with the Savitzky–Golay filter," *Remote Sens. Environ.*, vol. 217, pp. 244–257, Nov. 2018.

[56] X. Li, J. Xiao, and B. He, "Chlorophyll fluorescence observed by OCO-2 is strongly related to gross primary productivity estimated from flux towers in temperate forests," *Remote Sens. Environ.*, vol. 204, pp. 659–671, Jan. 2018.

[57] Z. Zhang *et al.*, "Reduction of structural impacts and distinction of photosynthetic pathways in a global estimation of GPP from space-borne solar-induced chlorophyll fluorescence," *Remote Sens. Environ.*, vol. 240, Apr. 2020, Art. no. 111722.

[58] Y. Zhang *et al.*, "A global moderate resolution dataset of gross primary production of vegetation for 2000–2016," *Sci. Data*, vol. 4, no. 1, Dec. 2017, Art. no. 170165.

[59] X. Yang *et al.*, "Solar-induced chlorophyll fluorescence that correlates with canopy photosynthesis on diurnal and seasonal scales in a temperate deciduous forest," *Geophys. Res. Lett.*, vol. 42, no. 8, pp. 2977–2987, 2015.

[60] H. Q. Liu and A. Huete, "A feedback based modification of the NDVI to minimize canopy background and atmospheric noise," *IEEE Trans. Geosci. Remote Sens.*, vol. 33, no. 2, pp. 457–465, Mar. 1995.

[61] J. D. Rodriguez, A. Perez, and J. A. Lozano, "Sensitivity analysis of $k$-fold cross validation in prediction error estimation," *IEEE Trans. Pattern Anal. Mach. Intell.*, vol. 32, no. 3, pp. 569–575, Mar. 2010.

[62] Q. Yuan *et al.*, "Deep learning in environmental remote sensing: Achievements and challenges," *Remote Sens. Environ.*, vol. 241, May 2020, Art. no. 111716.

[63] G. Duveiller and A. Cescatti, "Spatially downscaling sun-induced chlorophyll fluorescence leads to an improved temporal correlation with gross primary productivity," *Remote Sens. Environ.*, vol. 182, pp. 72–89, Sep. 2016.

[64] S. Hu and X. Mo, "Detecting regional GPP variations with statistically downscaled solar-induced chlorophyll fluorescence (SIF) based on GOME-2 and MODIS data," *Int. J. Remote Sens.*, vol. 41, no. 23, pp. 9206–9228, Dec. 2020.

[65] A. Porcar-Castell *et al.*, "Linking chlorophyll a fluorescence to photosynthesis for remote sensing applications: Mechanisms and challenges," *J. Exp. Botany*, vol. 65, no. 15, pp. 4065–4095, Aug. 2014.

[66] X. Liu *et al.*, "Downscaling of solar-induced chlorophyll fluorescence from canopy level to photosystem level using a random forest model," *Remote Sens. Environ.*, vol. 231, Sep. 2019, Art. no. 110772.

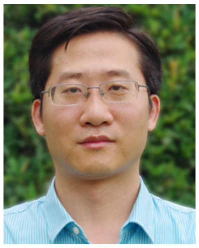

**Huanfeng Shen** (Senior Member, IEEE) received the B.S. degree in surveying and mapping engineering and the Ph.D. degree in photogrammetry and remote sensing from Wuhan University, Wuhan, China, in 2002 and 2007, respectively.

In 2007, he joined the School of Resource and Environmental Sciences (SRES), Wuhan University, where he is currently a Luojia Distinguished Professor and the Associate Dean. He was or is the Principal Investigator of two projects supported by the National Key Research and Development Program of China and six projects supported by the National Natural Science Foundation of China. He has authored over 100 research articles in peer-reviewed international journals. His research interests include remote sensing image processing, multisource data fusion, and intelligent environmental sensing.

Dr. Shen is a Council Member of the China Association of Remote Sensing Application, an Education Committee Member of the Chinese Society for Geodesy Photogrammetry and Cartography, and a Theory Committee Member of the Chinese Society for Geospatial Information Society. He is also a member of the Editorial Board of *Journal of Applied Remote Sensing* and *Geography and Geo-Information Science*.

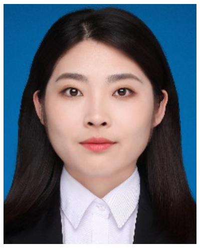

**Yuchen Wang** received the Bachelor's degree in geographic information science from Hohai University, Nanjing, China, in 2019. She is currently pursuing the Ph.D. degree in cartography and geographic information engineering with Wuhan University, Wuhan.

Her research interests mainly include the processing of multisource remote sensing images and their application in the terrestrial ecosystem and global change.

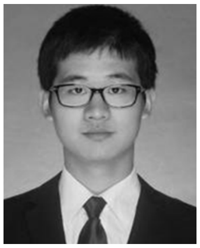

**Xiaobin Guan** received the B.S. and Ph.D. degrees in geographical information system from the School of Resource and Environmental Sciences, Wuhan University, Wuhan, China, in 2013 and 2018, respectively.

He is currently an Associate Researcher with the School of Resource and Environmental Sciences, Wuhan University. He has been a Post-Doctoral Fellow with Wuhan University and the University of Toronto, Toronto, ON, Canada. His research interests include the processing of multisource remote sensing images and their application in the terrestrial ecosystem and global change.

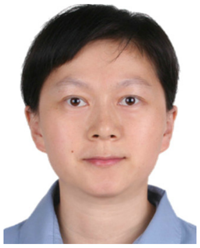

**Wenli Huang** (Member, IEEE) received the B.S. degree in geographic information system (computer cartography) from Wuhan University, Wuhan, China, in 2006, the M.S. degree in cartography and geographic information system from Beijing Normal University, Beijing, China, in 2009, and the Ph.D. degree in geographical sciences from the University of Maryland, College Park, MD, USA, in 2015.

From 2015 to 2018, she was a Post-Doctoral Research Associate with the Department of Geographical Sciences, University of Maryland. Since 2019, she has been an Associate Research Professor with the School of Resource and Environmental Sciences, Wuhan University. Her areas of interest include regional-to-national mapping of land cover and land use, forest canopy structures, and aboveground biomass through the fusion of multisource remotely sensed data.

**Jiajia Chen** received the M.E. degree in geomatics engineering from Wuhan University, Wuhan, China, in 2018, where she is currently pursuing the Ph.D. degree in cartography and geographic information engineering.

Her research interests mainly include atmospheric remote sensing, multisource data fusion, and ozone air pollution.

**Dekun Lin** received the M.E. degree in geomatics engineering from Wuhan University, Wuhan, China, in 2019, where he is currently pursuing the Ph.D. degree in cartography and geographic information engineering.

His research interests mainly include remote sensing information processing and environmental monitoring system development.

**Wenxia Gan** (Member, IEEE) was born in Hubei, China, in 1987. She received the B.S., M.S., and Ph.D. degrees in photogrammetry and remote sensing from Wuhan University, Wuhan, China, in 2009, 2011, and 2015, respectively.

She was a Visiting Scholar with The Ohio State University, Columbus, OH, USA, from 2018 to 2020. She is currently an Associate Professor with the School of Civil Engineering and Architecture, Wuhan Institute of Technology, Wuhan. Her research interests include radiometric normalization of remote sensing data and application of RS/GIS technique on ecology environment and civil engineering, i.e., the evaluation of the pavement condition index based on 3S.

Dr. Gan serves as a reviewer for several international journals in field photogrammetry and remote sensing.